npj | precision oncology

Article

Published in partnership with The Hormel Institute, University of Minnesota

https://doi.org/10.1038/s41698-024-00752-1

Single cell-spatial transcriptomics and bulk multi-omics analysis of heterogeneity and ecosystems in hepatocellular carcinoma

Jiazhou Ye[1,5], Yan Lin[2,5], Zhiling Liao[3], Xing Gao[2], Cheng Lu[1], Lu Lu[2], Julu Huang[1], Xi Huang[2], Shilin Huang[2], Hongping Yu[4], Tao Bai[1], Jie Chen[1], Xiaobo Wang[1], Mingzhi Xie[2], Min Luo[2], Jinyan Zhang[2], Feixiang Wu[1], Guobin Wu[1], Liang Ma[1], Bangde Xiang[1], Lequn Li[1], Yongqiang Li[2], Xiaoling Luo[4] ✉ & Rong Liang [2] ✉

This study profiled global single cell-spatial-bulk transcriptome landscapes of hepatocellular carcinoma (HCC) ecosystem from six HCC cases and a non-carcinoma liver control donor. We discovered that intratumoral heterogeneity mainly derived from HCC cells diversity and pervaded the genome-transcriptome-proteome-metabolome network. HCC cells are the core driving force of taming tumor-associated macrophages (TAMs) with pro-tumorigenic phenotypes for favor its dominant growth. Remarkably, M1-types TAMs had been characterized by disturbance of metabolism, poor antigen-presentation and immune-killing abilities. Besides, we found simultaneous cirrhotic and HCC lesions in an individual patient shared common origin and displayed parallel clone evolution via driving disparate immune reprograms for better environmental adaptation. Moreover, endothelial cells exhibited phenotypically conserved but executed differential functions in a space-dependent manner. Further, the spatiotemporal traits of rapid recurrence niche genes were identified and validated by immunohistochemistry. Our data unravels the great significance of HCC cells in shaping vibrant tumor ecosystems corresponding to clinical scenarios.

Hepatocellular carcinoma (HCC) is the sixth most common cancer and the fourth major cause of cancer-related death worldwide. Multiple etiological and pathogenic stimulation contribute to this lethal malignancy is characterized by a high degree of intratumoral heterogeneity (ITH)[1,2]. It is manifested not merely in the multi-omics traits including genomics, transcriptomics, proteomics, metabolomics, but also in the diverse morphological features and spatial distributions of cells, thereby forming various ecosystems such as specific tumor microenvironments (TME) and tumor immune microenvironments (TIME)[3–6].

HCC carcinogenesis and progression are the result of dynamic evolutionary processes. Despite inherent cellular heterogeneity had existed within the tumor cell clusters, greater heterogeneity can be introduced through environmental effects[7], with HCC cells playing core roles in such dynamic evolutionary networks. Persistent environmental stimulation usually causes diverse stochastic genetic and non-genetic alterations, leading to the emergence of multiple HCC subclusters that possess dynamic plasticity. These adaptive HCC subclusters selectively exhibit deterministic tumor characteristics for the remodeling of the ecosystem to favor their dominant growth by manipulating the surrounding cells' functions through the intricate signaling networks, thus increasing the diversity of cellular components and strengthening more signals that promote HCC heterogeneity[4,8,9]. Further, an evolutionary game of these preponderant HCC cell subclusters with the ecosystems distinctively drives the development of ITH, ultimately manifesting as varied clinicopathological characteristics and causing undesirable clinical outcomes of rapid disease progression, poor therapeutic response, and frequent recurrences[10,11]. Multitude of studies have elucidated highly cellular and biological heterogeneous, but the intrinsic relations and molecular mechanisms underlying

---

[1]Department of Hepatobiliary Surgery, Guangxi Medical University Cancer Hospital, Nanning, China. [2]Department of Digestive Oncology, Guangxi Medical University Cancer Hospital, Nanning, China. [3]Department of Pathology, Guangxi Medical University Cancer Hospital, Nanning, China. [4]Department of Experimental Research, Guangxi Medical University Cancer Hospital, Nanning, China. [5]These authors contributed equally: Jiazhou Ye, Yan Lin. ✉e-mail: luoxiaoling@gxmu.edu.cn; liangrong@gxmu.edu.cn

THE HORMEL INSTITUTE
UNIVERSITY OF MINNESOTA

the integration of ITH into specific clinical scenarios[12] corresponding to various pathological characteristics and clinical outcomes have not been clearly unraveled.

Traditional high-throughput omics studies just focused on the macroscopic analysis of the common features of mixed cell components. Emerging single-cell RNA sequencing (scRNA-seq) and spatial transcriptome sequencing (ST-seq) enable the acquisition of multilayer molecular information with unprecedented resolutions. scRNA-seq profiles the dynamic landscapes of cellular and genetic alterations in the temporal dimension[13], and effectively supplies the lack of single-cell resolution in ST technology caused by the inclusion of dozens of cells within a single spot. In contrast, ST-seq provides high-quality transcriptional data for visualization of the spatial dynamic landscape[14], breaking through the limitation of cell location information lost by scRNA-seq. It has been reported that scRNA-seq sheds light on the ITH, but spatial heterogeneity has rarely been discussed.

Here, we constructed a single cell-spatial-bulk global heterogeneity landscapes and spatiotemporal dynamic evolution of the ecosystem in HCC. We observed that ITH was mainly derived from the diversity of HCC cell subclusters possessing specific markers, which consistently pervaded the genome–transcriptome–proteome–metabolome network. Also, we demonstrated most immune cell subpopulations were shared among all patients but their proportions were significant different, and different spatial distribution of immune cells subpopulations were specifically contributing to the immune heterogeneity. In an individual patient, we identified the common progenitor cells shared by simultaneous cirrhosis and HCC and experienced parallel evolution, accompanying unique spatiotemporal dynamic pathway activities during ultimately led to their different pathological outcomes and immune reprogram by the lesions for the enhancement of better environmental adaptation. Further, we found endothelial cells (ENs) exhibited phenotypic conservatism but executive differential functions in a space-dependent manner. Moreover, we characterized specific ecological niche genes of rapid HCC recurrence on a spatiotemporal scale, and their prognostic value was validated in independent cohorts beyond 7000 patients. Our data unprecedentedly revealed the spatiotemporal dynamic landscape of HCC heterogeneity, and emphasized the great importance of HCC cells in shaping vibrant tumor ecosystems.

Results

Construction of dynamic spatiotemporal landscape of the ecosystem in HCC by integrated analysis of single cell-spatial RNA-Seq combined bulk multi-omics sequencing

Six HCC tissue and one cirrhotic tissue samples and preoperative blood samples were collected from six patients with pathological diagnosis. A non-carcinoma liver tissue and blood samples were obtained from one patient underwent surgical resection for hepatic hemangioma were used as control. These samples were subjected to scRNA-seq, ST-seq, whole exome sequencing, whole transcriptome sequencing, full-length transcriptome sequencing, proteome sequencing, and non-targeted metabolomics sequencing approaches (Fig. 1). Clinicopathological characteristics of all HCC patients and the control donor were detailed in Supplementary Fig. 1a-c. In particular, Patient#4 had simultaneous HCC (HCC4) and cirrhotic (CIR4) lesions. Highly angiogenesis (Microvascular density, MVD ≥ 50 vessels/200× high power field, HPF) was confirmed in the HCC lesions of Patients#3, #4, and #5 (HCC3, HCC4, and HCC5) by postoperative pathological examinations. Early recurrence occurred in Patient#5 with disease-free survival (DFS) of 9 months, and rapid recurrence occurred in Patient#2 with a DFS of 2 months.

After standardized data processing and quality control, a total of 25,624 high-quality spatial resolution spots and 81,698 high-quality single-cell transcriptional profiles were obtained. Fifty-five cell clusters were generated (Fig. 2a, Supplementary Fig. 1d) comprising 11 cell types, including HCC cells (glypican-3 *(GPC3)*, alpha-fetoprotein *(AFP)*), epithelial cells (cluster of differentiation 24 *(CD24)*, epithelial cell adhesion molecule *(EpCAM)*), and vascular endothelial cells (von willebrand factor *(VWF)*, cluster of differentiation 34 *(CD34)*). Positive markers of each cell clusters are agreed with the gene signatures identified in practice guidelines for standardized pathological diagnosis of HCC and recent scRNA-seq studies, supporting their phenotypes were consistent with the malignant features (Fig. 2b)[15,16] By integrating analysis of single cell-spatial RNA-Seq combined bulk multi-omics sequencing, we constructed global heterogeneity landscapes and spatiotemporal dynamic evolution pattern of the ecosystem in HCC corresponding to specific clinical scenarios of various pathological characteristics and clinical outcomes.

ITH was primarily derived from diverse types of HCC cells

The global spatiotemporal landscapes of the ecosystem in HCC revealed that ITH primarily arose from diverse types of HCC cells, while most immune and stromal cells (Neutrophils, $CD4^+$ T, $CD8^+$ T, monocyte-derived dendritic cells (MDDC), macrophage (Mas), and B cell) were shared among all the HCC patients (Fig. 2c–e). The unsupervised clustering at a high resolution of HCC cells and cirrhotic cells shows that HCC subclusters possessed specific positive markers in individuals (Fig. 3a–d), among which the oncogenes neuropeptide w *(NPW)* and interferon alpha inducible protein 27 *(IFI27)* were firstly discovered being novel markers for HCC[17,18]. Besides, lectin galactoside-binding soluble 3 *(LGALS4)*, regenerating islet-derived protein 1-alpha *(REG1A)*, and metallothionein 1G *(MT1G)* exhibited consistency in the transcriptome and proteome at the bulk level, implying the strong invasiveness of these HCC subclusters[19–21]. We then identified specific genes with a high confidence in each patient by multi-omics analysis approach (Fig. 3e). Intriguingly, metabolic heterogeneity was observed manifesting in HCC lesions and peripheral blood (Fig. 3f)[3,22]. In Patient#4, specific metabolites (20-hydroxyecdysone, dehydroepiandrosterone sulfate, cholesterol sulfate, etc.) were shared in cirrhotic nodule, HCC lesion, paracancerous tissue, and peripheral blood (Supplementary Table 1), implying a common pathophysiological molecular basis shared by cirrhosis and HCC. Overall, we demonstrated that ITH primarily derived from diverse types of HCC cells and consistently pervaded the genome-transcriptome-proteome-metabolome network.

A distinct tumor cells self-drive modulation of immune ecosystem in HCC

We constructed high-resolution single cell-spatial landscape mapping the immune ecology and identified eight types of immune cells (Fig. 4a, Supplementary Fig. 2a-c), including Macs (cluster of differentiation 68 *(CD68)*, cluster of differentiation 14 *(CD14)*, and human leukocyte antigen-DRA *(HLA-DRA)*), $CD8^+$ T cells (cluster of differentiation 3 delta *(CD3D)*, cluster of differentiation 274 *(CD247)*, and cluster of differentiation 8 alpha *(CD8A)*, and B cells (cluster of differentiation 79 alpha *(CD79A)* and membrane-spanning 4-domains a1 *(MS4A1)*). The Mac subpopulations mainly included the M0, M1 (fc gamma receptor Ia *(FCGR1A)*), and M2 (macrophage scavenger receptor 1 *(MSR1)*, cluster of differentiation 163 *(CD163)*, and cluster of differentiation 209 *(CD209)* cells. The $CD8^+$ T cells included virgin, cytotoxic (granulysin *(GNLY)*, interferon gamma *(IFNG)*, and granzyme b *(GZMB)*), and exhausted $CD8^+$ T (cytotoxic t-lymphocyte associated protein 4 *(CTLA4)*, lymphocyte activating 3 *(LAG3)*, and programmed cell death 1 *(PDCD1)*) cells (Fig. 4b, c, Supplementary Fig. 2d-f). Notably, although most immune cell populations appeared to be shared among patients, ST-seq precisely displayed the differential distribution of the cellular activity signals in individual, which specifically contributed to the immune heterogeneity (Fig. 2c, d, Fig. 4d–g, Supplementary Fig. 2a-c).

We found aberrant signals that enhance T cell differentiation, immunity, and inflammation in Mac and $CD8^+$ T cells (Supplementary Fig. 2g-h). M1-type tumor-associated macrophages (TAMs) were numerically dominant and exhibited high metabolic activities of canonical glycolytic (enolase 1 *(ENO1)*, glyceraldehyde-3-phosphate dehydrogenase *(GAPDH)*, and lactate dehydrogenase a *(LDHA)*) and amino acid metabolism, but inactivated immune cytotoxicity and antigen presentation pathways were observed. These aberrant metabolic signaling were accompanied by phenotypic changes in TAMs[23] specifically led to impairment of the antitumor

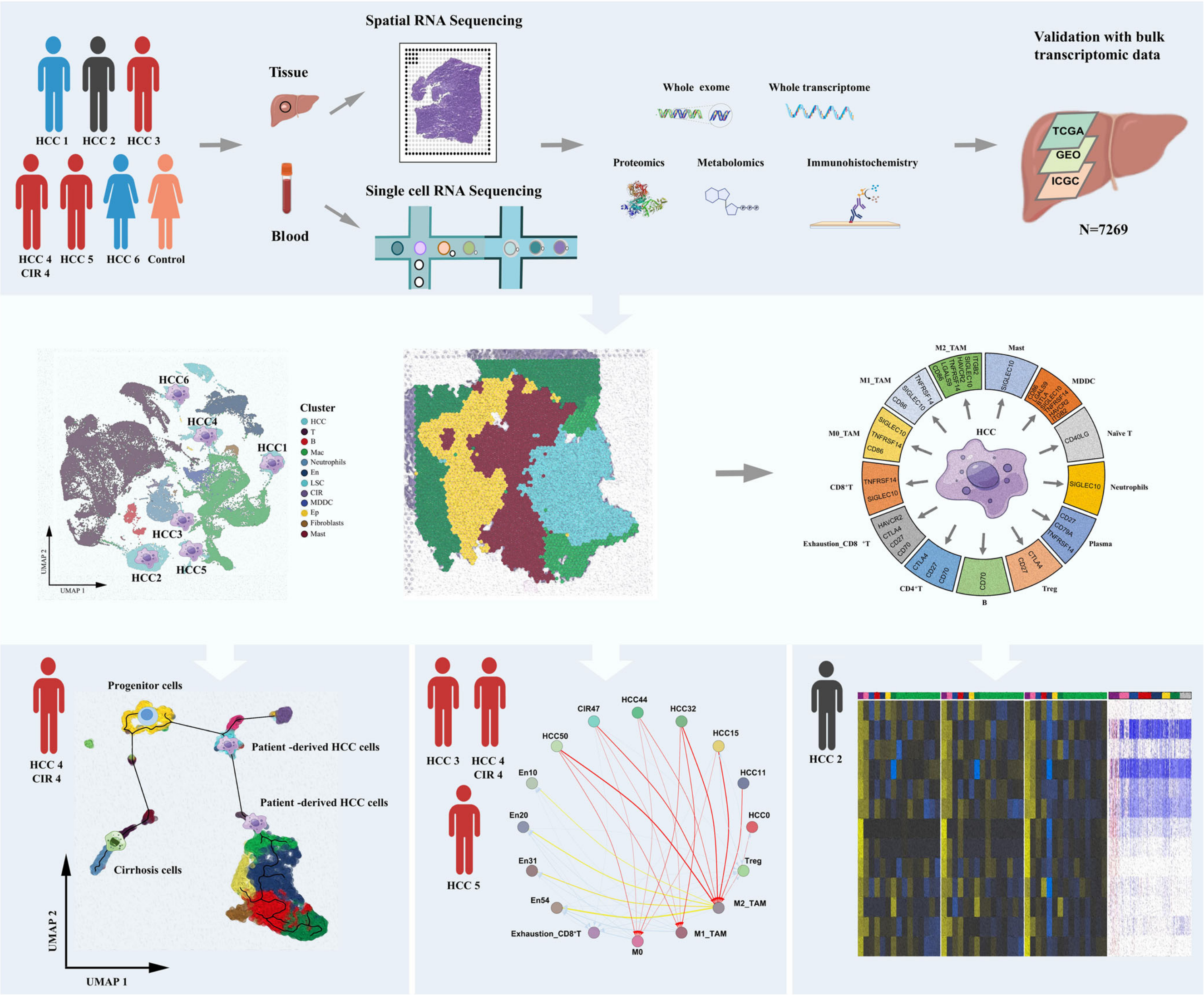

Fig. 1 | Single cell-spatial-bulk multi-omics analysis profiled the global heterogeneity landscapes and spatiotemporal dynamic evolution of the ecosystem in HCC.

functions of M1-TAMs, and enhancement of signaling cascades for metabolites lipids and amino acid of the M2-TAMs to promote immunosuppression (Supplementary Table 2)[24–26]. Although the cytotoxic T cells were significantly outnumbered the exhausted T cells, but highly expressed key immunosuppressive factors transforming growth factor beta 1 *(TGF-β1)*, c-c motif chemokine ligand 4 *(CCL4)*, and nuclear factor kappa-light-chain-enhancer of activated b cells *(NF-κB1)* to activate the T cell receptor signaling pathways, transcriptional misregulation in cancer pathways, apoptosis pathways, programmed cell death protein-ligand 1 *(PD-L1)* expression and programmed cell death protein 1 *(PD-1)* checkpoint pathway in cancer (Supplementary Table 3). It suggested that cytotoxic CD8$^+$ T cells under multiple pressures, such as continuous tumor antigens stimulation, have actually degenerated into dysregulated transcription, immunosuppression, and susceptibility to apoptosis, which is consistent with the findings of Philip et al. [27] and Sun et al. [15]. Overexpression of immune checkpoint genes *CTLA4*, *PDCD1*, and t cell immunoreceptor with immunoglobulin and itim domains *(TIGIT)* were observed concentrated on exhausted CD8$^+$ T, CD4$^+$ T, and Treg cells (Fig. 4h), indicating the environmental-mediated immunosuppression. Next, HCC-immune cells communication network was constructed (Fig. 4i–j), revealing widespread intracellular communications initiated by HCC cells. Specifically, the most frequent intracellular communication events were observed between HCC and Macs clusters, underlying the core status of Macs in TIME[28]. In particular, we demonstrated M2-TAMs interacted with Tregs through the cluster of differentiation 86 (CD86) receptor-CTLA4 ligand axis and the colocalization of *CD86* and *CTLA4* was clearly corroborated by the spatial resolution map (Fig. 4k). This foundlings implied M2-TAMs may serve as core regulators in the modification of TIME driven by HCC. Meanwhile, macrophage-dendritic cells (MMDCs) interacted with Tregs to promote CD8$^+$ T cell exhaustion.

Simultaneous cirrhotic and HCC lesions share progenitor cells and evolve in parallel

In general, HCC occurs in the setting of liver cirrhosis[29]. In a single individual Patient#4, we obtained valuable specimens of simultaneous cirrhotic (CIR4) and HCC (HCC4) lesions (Fig. 5a) and explored the spatiotemporal evolution patterns of lesions with a high risk for carcinogenesis (cirrhosis) and HCC. We found CIR4 and HCC4 cells shared more copy number variation (CNV) landscapes at the genomic level (Fig. 5b), indicating they share a common evolutionary origin[30]. At the transcriptome level, HCC4 and CIR4 cells were extracted for unsupervised clustering and 15 cell subclusters were captured (Fig. 5c). These subclusters underwent continuous development processes (Fig. 5d) since C0 location, which is the earliest origin of the developmental trajectory locate the common progenitor cells of the two types of lesions (Supplementary Table 4). It significantly activated the gene module 1 which was enriched with dual signals of hepatic disease

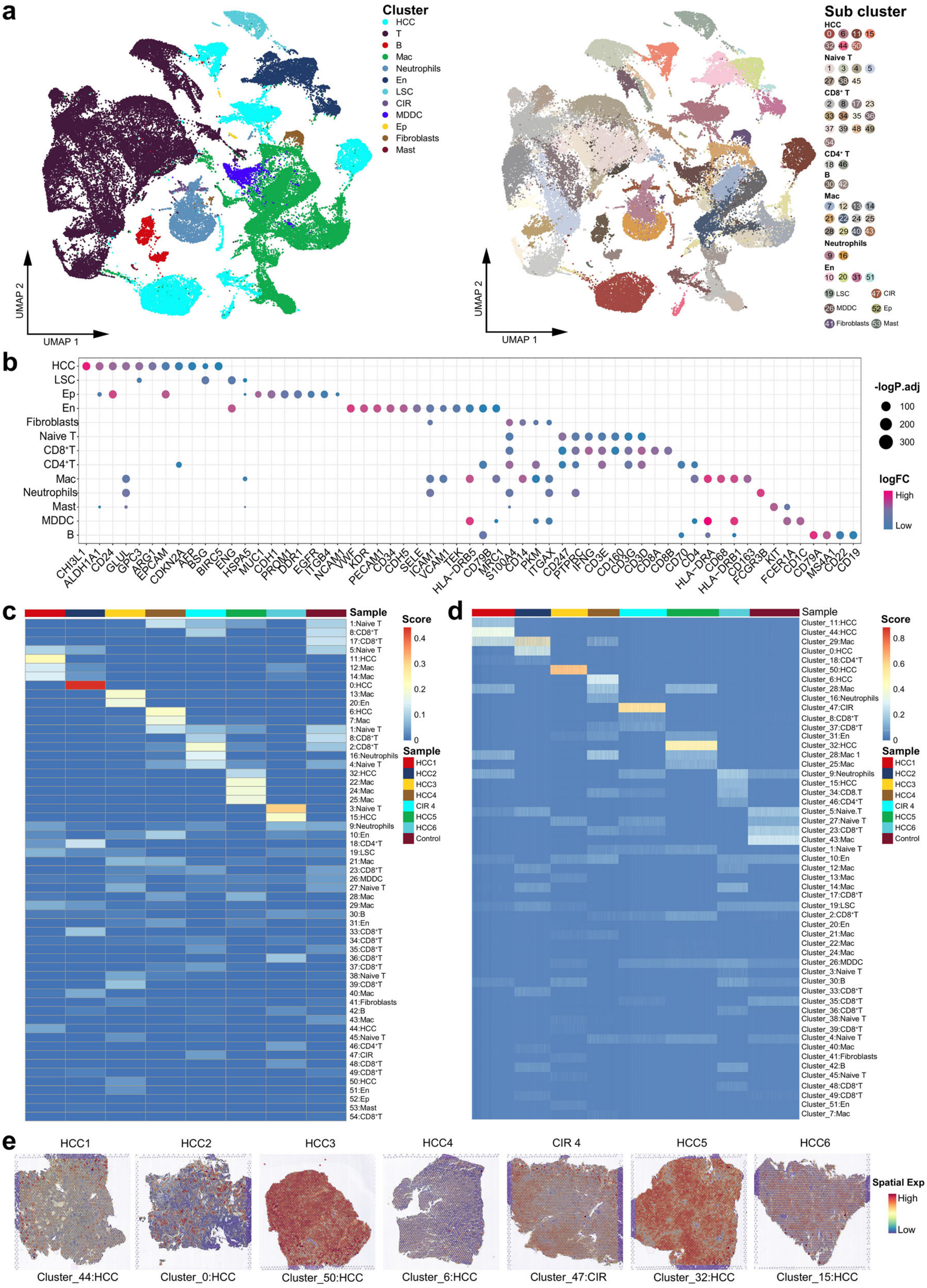

Fig. 2 | Spatiotemporal globe landscapes of the ecosystem in HCC, cirrhosis, and non-carcinoma liver. a Uniform Manifold Approximation and Projection (UMAP) plot showing the cell types in all the study samples, with different color codes denoting different cell clusters (left) and subclusters (right). **b** Bubble chart showing the specific markers of each cell cluster. **c** Heatmap representing the proportions of different cell types of each study sample at the single-cell level. **d** Heatmap representing the proportions of different cell types of each study sample on the spatial resolution. **e** Spatial feature plot showing the specific cell clusters of each HCC and CIR lesion. See also Supplementary Fig. 1.

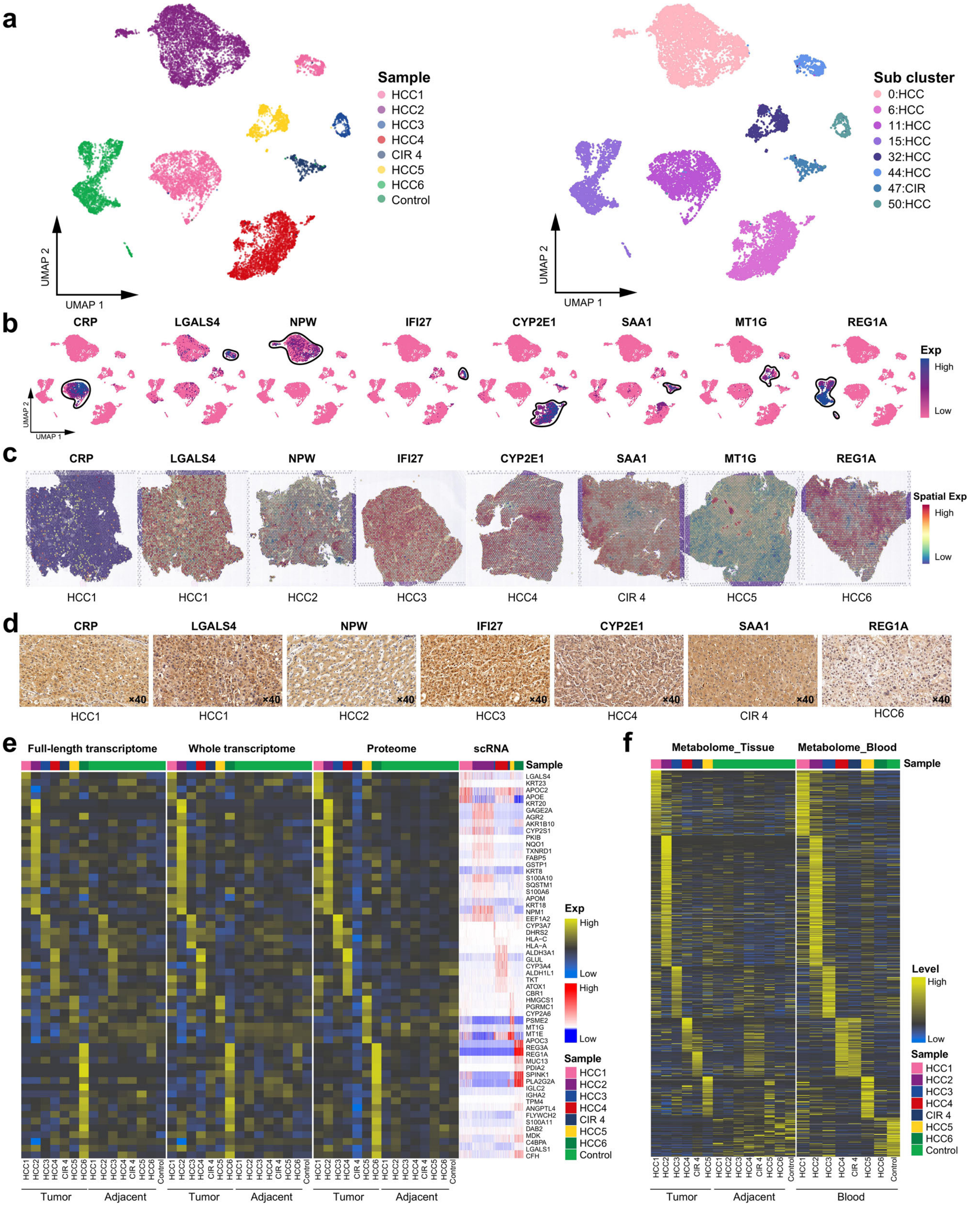

Fig. 3 | Spatiotemporal intratumor heterogeneities in HCC and cirrhosis. **a** UMAP plot showing the HCC and CIR cell types, with different color-codes denoting lesions origin (left) and cell subclusters (right). **b**, **c** UMAP plot and spatial feature plots showing the distribution of specific markers on the cell subclusters from Fig. 2A (right). **d** Immunohistochemical validation of the expression of specific markers, the scale bars represent 20 μm. **e** Heatmap representing the average expression of specific markers of each cell subcluster at the full-length transcriptome, whole transcriptome, proteome, and scRNA levels. **f** Heatmap representing the levels of metabolic changes in the tissues and blood of HCC patients and control donor. See also Supplementary Table 1.

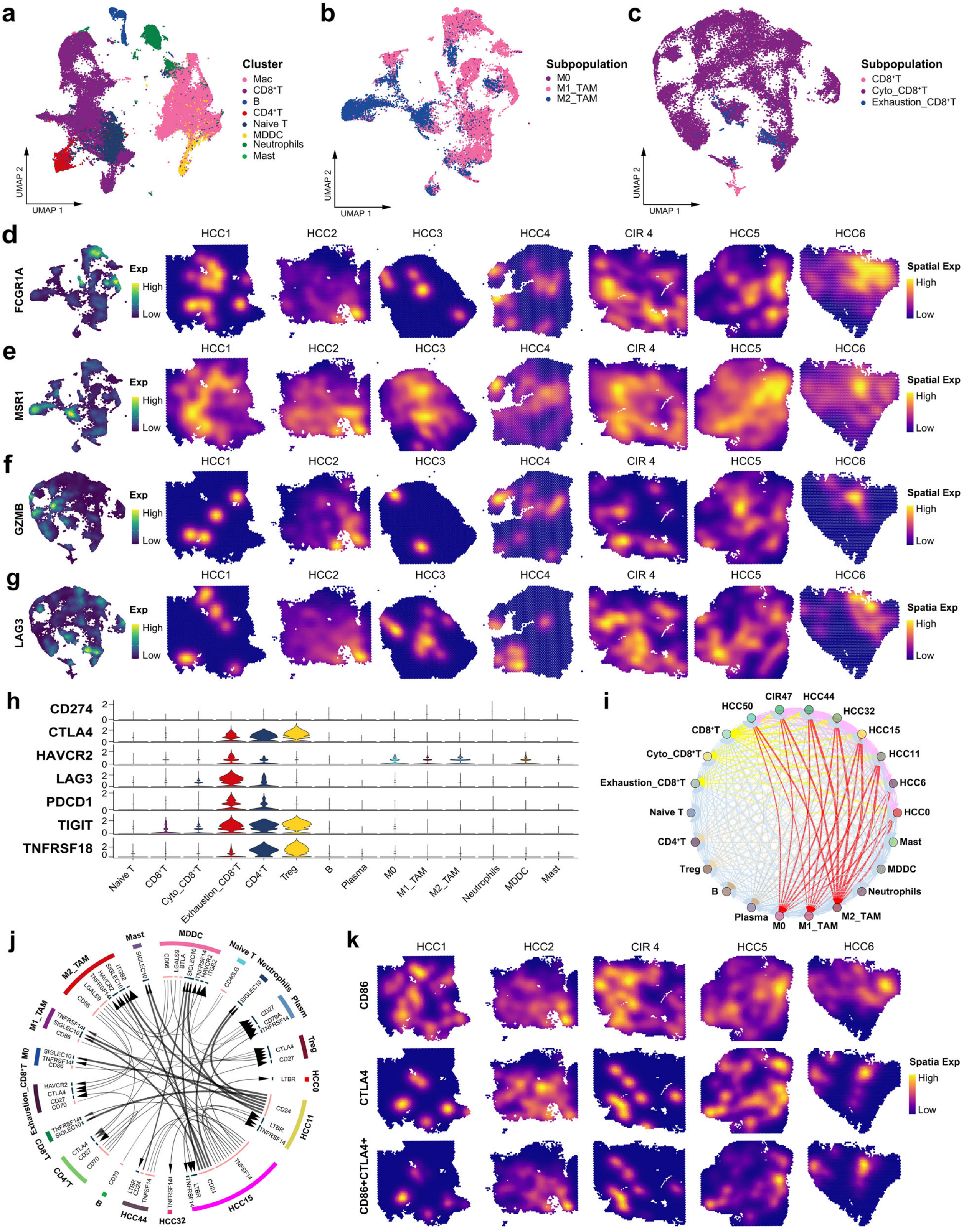

and HCC (Fig. 5e, Supplementary Table 5). Transcriptional activation of different downstream gene modules led to discrepant pathological outcomes: activation of a series of hepatic disease signals in gene module 2 resulted in cirrhosis; whereas activation of carcinogenesis and malignant proliferation signals in the gene modules 3, 4, and 5 promoted HCC. Spatial resolution map showed significant differences in differentiation trajectories of progenitor cells developed to HCC4 and CIR4 (Fig. 5f). Cirrhotic nodules were rich in an abundance of hepatic disease signaling spatial blocks but fewer carcinogenic signaling spatial blocks, while numerous chemical carcinogenic, metabolic, invasion, and immune signaling spatial blocks were observed in HCC lesions (Fig. 5g). The antigen processing and presentation signaling pathways were activated in both the cirrhotic and HCC spatial

Fig. 4 | Spatiotemporal characteristics of the immune microenvironment in HCC and cirrhosis. a UMAP plot showing the immune cell clusters in all the study samples, labeling in different colors. UMAP plot showing the subpopulations of macrophages (**b**) and CD8$^+$ T cells (**c**) in all the study samples, labeling in different colors. UMAP plot and spatial feature plot showing the visualized distribution of specific markers for M1-TAMs (**d**) and M2-TAMs (**e**). UMAP plot and spatial feature plot showing the visualized distribution of specific markers for cytotoxic CD8$^+$ T cells (**f**) and exhausted CD8$^+$ T cells (**g**). **h** Violin plot showing the expression of immune checkpoints molecules on each immune cells. **i** Bubble plot showing the intercellular communications among HCC cell, CIR cell, and immune cell subpopulations, with each bubble denoting the cell identity and line thickness denoting the strength of intercellular interactions. **j** Circos plot showing the Intercellular communication network of HCC cell, CIR cell, and immune cell subpopulations with a high confidence level, with each arrow denoting the interaction between the source cell ligand and target cell receptor, and the arrow thickness denoting the number of ligand-receptor interaction pairs. **k** Spatial feature plot showing the distribution of the co-expression of CD86, CTLA4, and CD86$^+$CTLA4. See also Supplementary Fig. 2, Supplementary Table 2 and Supplementary Table 3.

blocks, but exhausted immune signals were only present in the HCC spatial blocks (Fig. 5g). A gene regulatory network (GRN) of HCC4 and CIR4 subclusters was constructed and organized into six functional transcription factors (TFs) modules, comprising runt-related transcription factor 2 *(RUNX2)*, retinoid x receptor alpha *(RXRA)*, transcription factor ap-4 *(TFAP4)*, and nuclear receptor subfamily 2 group f member 2 *(NR2F2)* served as the core specific TFs (Fig. 5h). These TFs exhibited stemness and proliferative features that favored evolution[31–34]. They expressed sequentially at different spatiotemporal nodes of destiny selection and correspondingly regulated the transcription of specific genes (Fig. 5i, j), providing guidance for the transformation of cell state and ultimately mediating the formation of the aforementioned cluster structures.

Dynamic reprogramming of the immune microenvironment accompanying the evolution of HCC and cirrhosis

Disease progression is a complex and dynamic process driven by the interaction between clonal evolution and immune reprogram[35,36], as confirmed in previous analysis. We deeply analyzed the immune ecology in Patient#4 (Fig. 6a) and particularly investigated the structure and differentiation trajectories of TAMs and CD8$^+$ T cells accompanying the evolution.

Macs underwent a continuous development process, starting from M0 cluster and differentiating into nine subpopulations (Fig. 6b, c) of each with specific markers (Supplementary Fig. 3a). We observed that TAMs surrounding HCC cells manifested high complexity of phenotypic plasticity through the evolution process (Supplementary Table 6). M0-TAMs located at the earliest origin of the developmental trajectory and comprised the common progenitor cells shared by CIR4 and HCC4. Normally, the mitochondrial pathway plays important roles in the M2-TAMs polarization[37,38], however, we found M0-TAMs had exhibited significant upregulation of multiple mitochondrial family genes *(MT-ND* family, mitochondrially encoded adenosine triphosphate synthase membrane subunit 6 *(MT-ATP6)*, mitochondrially encoded cytochrome b *(MT-CYB)*, and mitochondrially encoded cytochrome c oxidase *(MT-CO)*), suggesting that mitochondrial energy metabolic reprogramming in this patient was initiated in the early stage of evolution. Chronologically, M0-TAMs differentiated into three types of M1 subtypes (Fig. 6c, Supplementary Table 6). According to the pseudo time series, the first subtype of M1-TAMs was positive for ribonuclease a family member 1, pancreatic *(RNASE1)* and specific to HCC lesions, locating at the earliest stage of clonal evolution. This RNASE1$^+$M1-TAMs mediated the IL-17 signaling pathway, cholesterol metabolism pathway, growth hormone synthesis, secretion and action signaling pathways, T-helper (Th) 1 and Th2 cells differentiation pathways through the oncogene *FOS*/*JUN*; but did not release pro-inflammatory factors, immune activators, and chemokines. These results indicated that the M1-TAMs surrounding the HCC lesion had lost the canonical glycolytic phenotype, as well as pro-inflammatory[39], immune-activating, and phagocytic functions start off with the early polarization. The second subtype of M1-TAMs strongly expressed galectin 3 *(LGALS3)* and was shared by the HCC and CIR lesions. These LGALS3$^+$M1-TAMs were characterized by the activation of cholesterol metabolism pathway, oxidative phosphorylation pathway, glycolysis pathway, hypoxia inducible factor 1 *(HIF-1)* signaling pathway, suggesting these cells had manifested higher metabolic disorders. Then it continuously differentiated along with the evolution with a split pattern. Around the HCC lesion, the LGALS3$^+$M1-TAMs were differentiated into the LGALS3$^+$MT1H$^+$MT1G$^+$M1-TAMs specifically overexpressed multiple metallothionein family genes, which are closely associated with the formation of M2 polarization that promote tumor growth and immunosuppression[40,41]. Meanwhile, stronger metabolic dysregulation was observed in these M1-TAMs. In the other way, the LGALS3$^+$M1-TAMs were differentiated into the KRAS$^+$LILRA2$^+$M2-TAMs shared by CIR and HCC lesions, which could activate phagosome signaling pathway, endocytosis signaling pathway, NF-κB signaling pathway, PD-L1 expression and PD-1 checkpoint pathway in cancer through secretion of M2 polarizing cytokines (c-c motif chemokine ligand 20 *(CCL20)*, c-type lectin domain containing 7a *(CLEC7A)*, transforming growth factor beta 1 *(TGFB1)*, interleukin 1 receptor antagonist *(IL1RN)*) and anti-inflammatory factors (tumor necrosis factor receptor superfamily member 1b *(TNFRSF1B)*)[42] for the exertion of phagocytosis, immunosuppression, and tissue remodeling liking as the functions of M2-TAMs[43,44]. The third subtype of M1-TAMs strongly expressed c-c motif chemokine ligand 2 *(CCL2)* and was mainly distributed around the HCC lesion. These CCL2$^+$M1-TAMs differentiated into an intermediate state characterized by CXCL1$^+$M1-TAMs which promoted the secretion of substantial amounts of cytokines and chemokines to increase tumor growth, metastasis, angiogenesis, immune escape; and activated the cytokine-cytokine receptor interaction signaling pathway, chemokine signaling pathway, transcriptional misregulation in cancer signaling pathway, PD-L1 expression and PD-1 checkpoint pathway in cancer, and apoptosis signaling pathway. These findings suggested that the CCL2$^+$M1-TAMs have exhibited oncogenic and immunosuppressive phenotypes under the uncontrolled inflammatory cytokine storms[45]. At the end of the pseudo time series trajectory there were the EBI3$^+$MARCO$^+$M2-TAMs, which was mainly around the CIR lesion, and retained partial phagocytotic and tissue remodeling functions as similar to the above-mentioned KRAS$^+$LILRA2$^+$M2-TAMs.

We then described the spatiotemporal characteristics of CD8 + T cells differentiation accompanying the evolution of CIR4 and HCC4 (Fig. 6d, e), with alterations of key markers on CD8$^+$ T cells during the evolution of the lesion cells (Supplementary Fig. 3b, Supplementary Table 7). GZMB$^+$GNLY$^+$TMPO$^+$CD8$^+$ T cells are present at the origin of pseudo time series of both the lesions, and strongly express several proliferation-related genes, such as ras homolog family member a *(RHOA)*, actin beta *(ACTB)*, and cyclin a2 *(CCNA2)* etc., involved in the regulation of cell cycle signaling pathway, mitosis signaling pathway, and actin cytoskeleton signaling pathway[46–48], indicating that these cells have high potential for proliferation, cytotoxic and migration. Then CD8$^+$ T cells in both HCC4 and CIR4 lesions all experienced a cytotoxic state characterized by RGS1$^+$CD8$^+$ T cells, which significant downregulated the proliferation-related genes but upregulated the antigen processing and presentation genes, and activated the Th1 and Th2 cell differentiation signaling pathway and T cell receptor signaling pathway, indicating acquired immunity was activated in the cytotoxic RGS1$^+$CD8$^+$ T cells. Subsequently, CD8$^+$ T cells around the HCC lesion evolved into a cytotoxic state characterized by XCL1$^+$CD8$^+$ T cells, in particular, in which numerous pro-apoptotic molecules and immunosuppressive factors (including fc fragment of immunoglobulin e receptor immunoglobulin *(FCER1G)*, *NF-κB1*, c-c motif chemokine ligand 3 *(CCL3)*, and c-c motif chemokine ligand 4 *(CCL4)*) were significantly

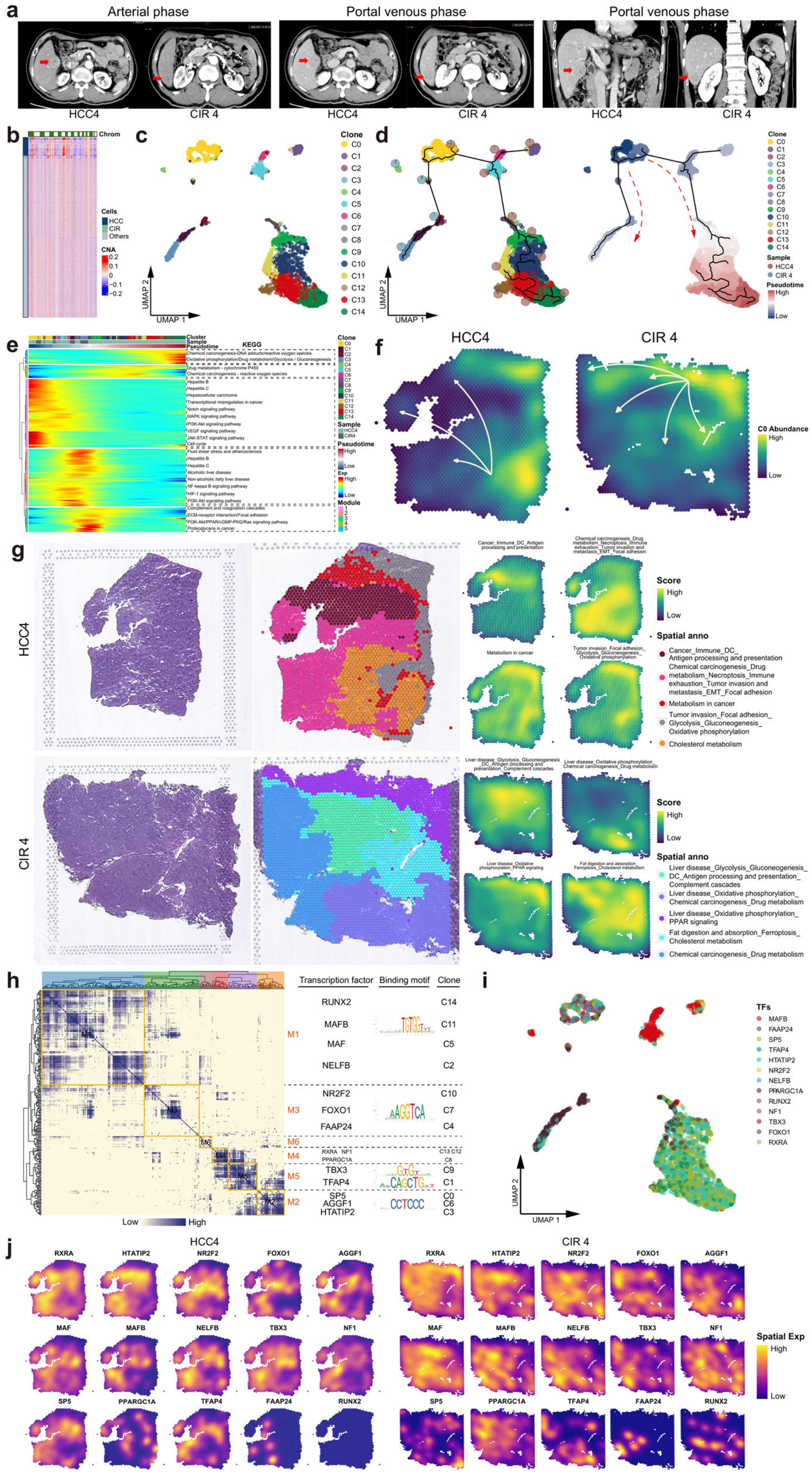

Fig. 5 | Parallel patterns of the evolution between HCC and cirrhosis. **a** Contrast-enhanced CT images of simultaneous HCC and CIR lesions in Patient #4. **b** Heatmap profiling the chromosome copy number variation (CNV) of HCC, CIR, and other cells of Patient #4. **c** UMAP plot showing the subclusters of HCC4 and CIR4 cells, labeling in different colors. **d** UMAP plot showing the pseudo-time series evolutionary patterns of the subclusters of HCC4 and CIR4. Pie chart showing the proportions of HCC4 and CIR4 cells in each subclusters. Pseudotime values (low to high) indicating the direction of sub-clonal evolution. **e** Heatmap representing the pseudo-time series of changes of differentially expressed genes in HCC4 and CIR4 subclusters. These genes were clustered into five modules, with each module participating in significantly different pathways. **f** Spatial feature plot showing the evolution patterns of HCC4 and CIR4 subclusters, with arrows indicating the direction of evolution. **g** H&E staining (left), and spatial cluster distribution of section (middle) labeled by colors, and density plots of specific gene sets of spatial cluster (right) for the HCC4 and CIR4, defined into different spatial blocks. (**h**) Heatmap representing the gene regulatory networks (GRNs) of HCC4 and CIR4 subclusters. Left: Identification of regulon modules based on the connection specificity index (CSI) matrix of regulons; Middle: Representative transcription factors (TFs) of modules and their binding motifs; Right: Relationships of modules with the HCC4 and CIR4 subclusters. **i** UMAP plot identifying the TFs that regulate HCC4 and CIR4 cell subclusters. **j** Spatial feature plot showing the distribution of TFs that regulate the HCC4 and CIR4 subclusters. See also Supplementary Table 4 and Supplementary Table 5.

upregulated[49–52], indicating that these cytotoxic XCL1$^+$CD8$^+$ T cells were actually in a dysfunctional state with low clonal expansion and immunosuppression. At the end of the pseudo time series were abundant GZMB$^+$GNLY$^+$CD8$^+$ T cells and a few exhausted T cells. Furthermore, apoptotic signaling was observed significantly inhibited in the GZMB$^+$GNLY$^+$CD8$^+$ T cells but was accompanied by an intense release of immunosuppressive factors (*LGALS1* and *CD47*)[53–56], indicating these CD8$^+$ T cells actually maintaining the persistent immunosuppression.

The dynamic characteristics of the immune microenvironment driven by HCC and CIR are distinct. The most frequent intermediate state in CIR was characterized by exhausted RGS1$^+$VCAM1$^+$CRTAM$^+$CD8$^+$ T cells. However, these cells reverted to the cytotoxic state characterized by

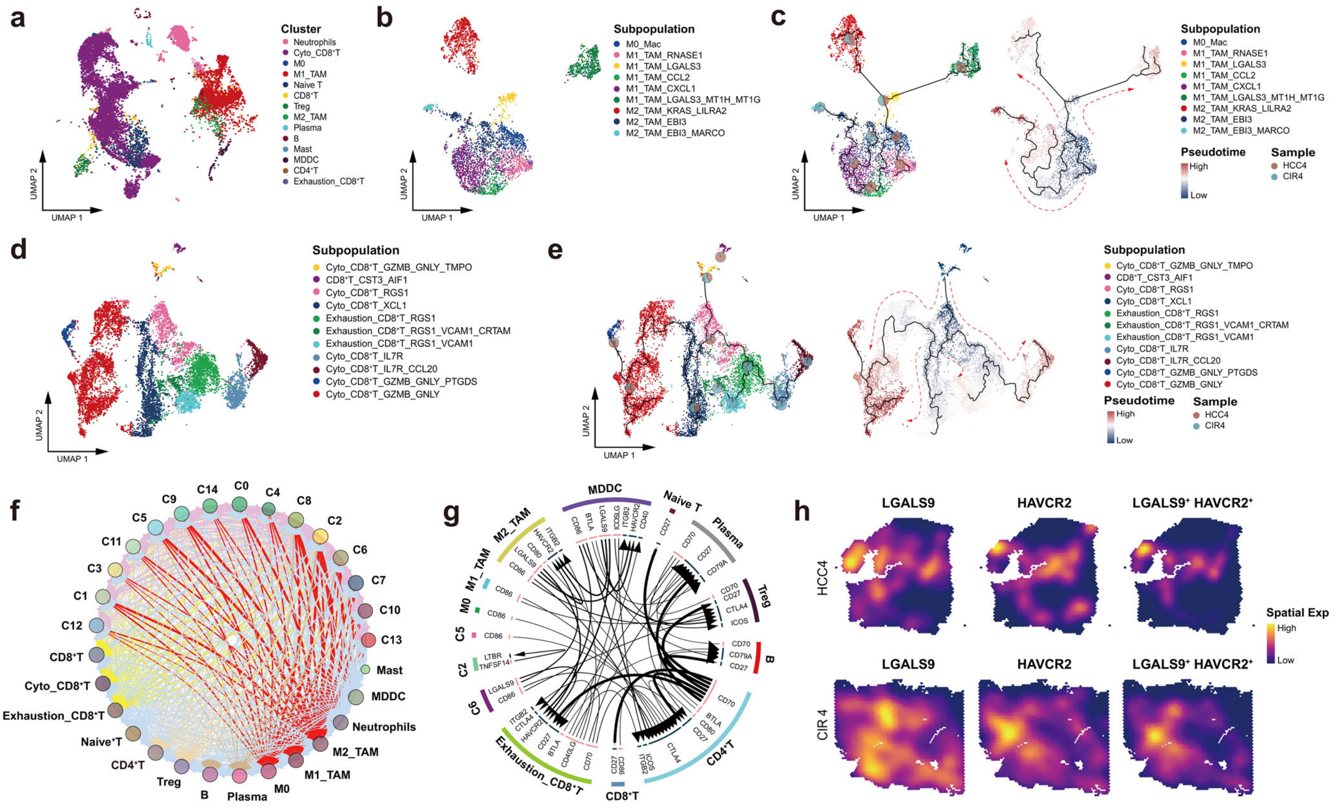

Fig. 6 | Dynamic reprogramming of the immune microenvironment accompanying the evolution of HCC and cirrhosis. a UMAP plot showing the immune cell clusters of HCC4 and CIR4, labeling in different colors. **b** UMAP plot showing the subpopulations of macrophages of HCC4 and CIR4, labeling in different colors. **c** Pseudo-time series of macrophages polarization in HCC4 and CIR4, Macrophages subpopulations are labeled by colors. Pie chart showing the proportion of macrophage subpopulations. **d** UMAP plot showing the $CD8^+$ T cell subpopulations of HCC4 and CIR4, labeling in different colors. **e** Pseudo-time series of $CD8^+$ T cell states in HCC4 and CIR4. $CD8^+$ T cell subpopulations are labeled by colors. Pie chart showing the proportion of $CD8^+$ T cells subpopulations. **f** Bubble plot showing the intercellular communications among the HCC cell, CIR cell, and immune cell subpopulations, with each bubble denoting the cell identity and line thickness denoting the strength of intercellular interactions. **g** Circos plot showing intercellular communication network of each HCC cell, CIR cell, and immune cell subpopulations with a high confidence level, with each arrow denoting the interaction between the source cell ligand and the target cell receptor, and the arrow thickness denoting the number of ligand-receptor interaction pairs. **h** Spatial feature plot showing the distribution of the co-expression of LGALS9, HAVCR2, and $LGALS9^+$HAVCR2 in HCC4 and CIR4. See also Supplementary Fig. 3, Supplementary Table 6 and Supplementary Table 7.

$IL7R^+CCL20^+CD8^+$ T cells, which mainly upregulated the T cell activation-related genes (human leukocyte antigen a *(HLA-A)*, cluster of differentiation *(CD28)*) pathway[57,58], and activated immune regulatory pathways such as the T cell receptor signaling pathway[59], antigen processing and presentation pathway[60], and Toll-like receptor signaling pathway[61] (Supplementary Fig. 3c, d).

TAMs remained displaying the highest frequency of communication with HCC cells in this patient (Fig. 6f, g), corroborating our findings from the global immune landscape (Fig. 4i). Notably, we constructed cellular communications between HCC and immune cells and found that HCC cells directly tamed exhausted $CD8^+$ T cells through the hepatitis a virus cellular receptor 2 (HAVCR2)-galectinl 9 (GALS9) and CD86-CTLA4 axes. Colocalization of these receptor-ligand axes was clearly corroborated by the spatial transcriptomic maps (Fig. 6h).

HCC drove epithelial cells reprogramming and regulated spatial distribution of vascular ecology

HCC is distinctive in its hypervascular nature[22]. The postoperative histology confirmed that angiogenesis was extremely strong in HCC3, HCC4, and HCC5. Our spatial transcriptomic maps showed that the focal adhesion signaling pathway was activated in all three HCC tissues (Fig. 5g, Fig. 7a, b). In addition, an active epithelial-mesenchymal transition (EMT)-related signal was found in HCC3 and HCC4, while strong HIF-1 signaling in HCC5, indicating that the spatiotemporal characteristics of HCC angiogenesis were similar but not fully identical. Patient#5 experienced early recurrence, whereas Patients#3 and #4 remained tumor-free until the end of follow-up. These results shed light on the great significance of hypoxia-related regulatory mechanisms affecting HCC angiogenesis and enhance the risk of early recurrence. Furthermore, among HCC3, HCC4, and HCC5 only four En sub-populations (Fig. 7c) with similar En activation-related functional pathways (Supplementary Fig. 4a) were identified, and relevant specific markers of each En sub-populations were mapped on the spatiotemporal landscapes (Fig. 7d, e). In particular, among which cytochrome p450 family 2 subfamily e member 1 *(CYP2E1)* was the most unique marker of both the HCC and En cells sub-populations of Patient#4 (Fig. 3b). Thus, we speculated there was a potential association of ectopic gene expression between HCC and En cells (Supplementary Table 8). We then investigated the expression of exosome marker genes cluster of differentiation 9 *(CD9)*, cluster of differentiation 63 *(CD63)*, and cluster of differentiation 81 *(CD81)* in HCC and En cell subpopulations and surprised that they were significantly overexpressed (Supplementary Fig. 4b). These findings indicated that HCC cells and En cells are highly likely to realize intercellular communication through exosomes for the promotion of constructing the vascular ecological niche; i.e., HCC cells promoted the specific reprogramming of Ens in Patient#4. In addition, we demonstrated that the ligand-receptor interactions in intercellular communication networks contributed to Ens reprogramming shared among all the patients, in which HCC subclusters served as the initiation to dominate TAMs served as hub for arouse a cascade

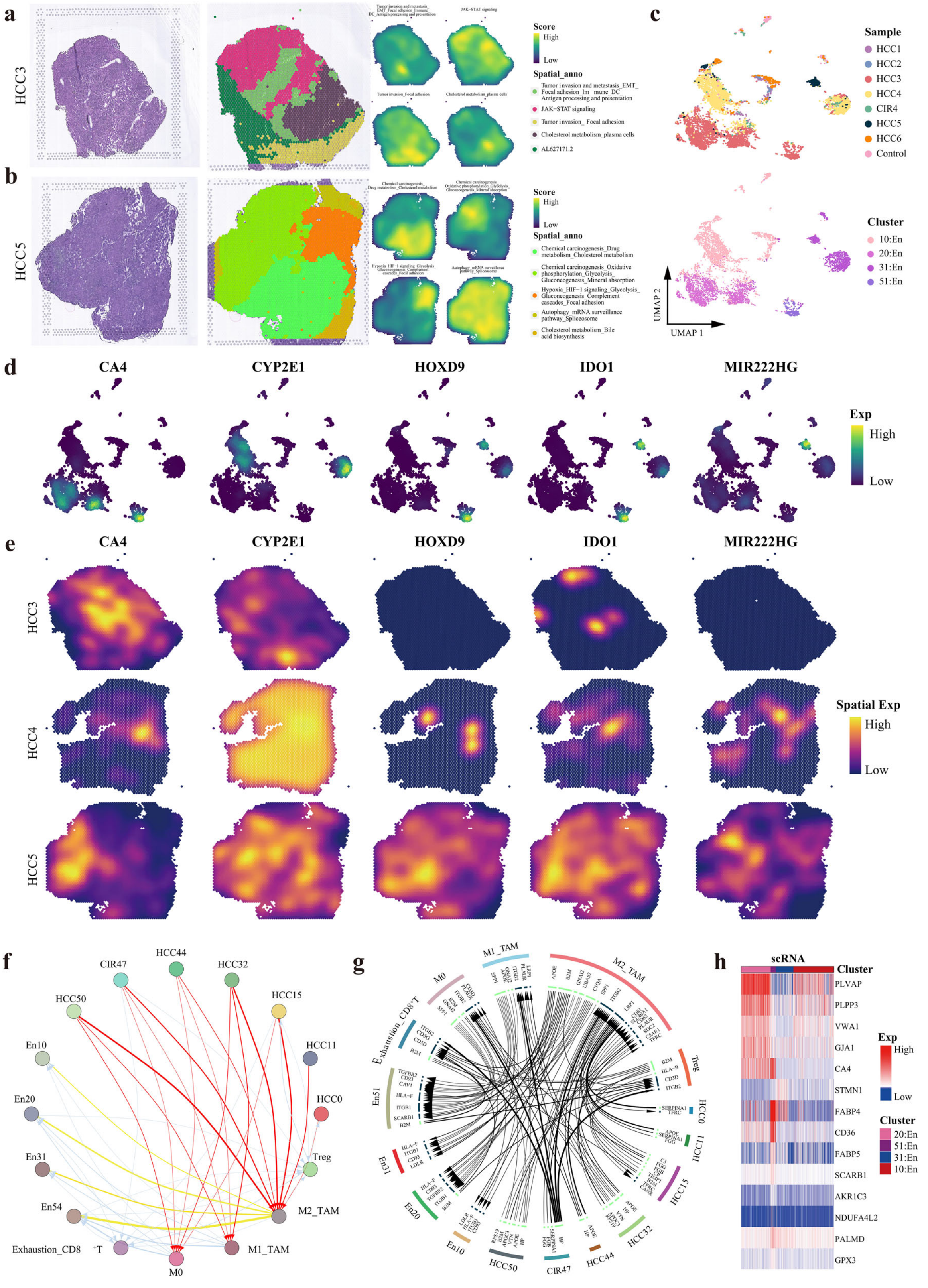

regulatory immunosuppression (Fig. 7f, g). Then, a GRN of En subpopulations was constructed and organized into seven modules (Supplementary Fig. 4c), comprising TFs human immunodeficiency virus type I enhancer-binding protein 1 *(HIVEP1)*, zinc finger protein 585A *(ZNF585A)*, homeobox protein hox-b5 *(HOXB5)*, and sterol regulatory element binding transcription factor 1 *(SREBF1)*. *HOXB5* and *SREBF1* have already been reported to play important roles in promoting En cell migration and proliferation, and stimulating vascular remodeling[62,63]. *HIVEP1* and *ZNF585A* are newly discovered tumor vascular endothelial TFs in this study and observed clearly expressed in spatial blocks (Supplementary Fig.

Fig. 7 | Ecological niche of angiogenesis in HCC. H&E staining(left), and spatial cluster distribution of section (middle) labeled by colors, and density plots of specific gene sets of spatial cluster (right) for HCC3 (**a**) and HCC5 (**b**), defined into different spatial blocks. **c** UMAP plot showing the endothelial cells for HCC3, HCC4 and HCC5, with different colors-codes denoting lesions origin (upper) and cell clusters (down). **d** UMAP plot showing the distribution of specific markers of each endothelial cell subclusters. **e** Spatial feature plots showing the expression of selected markers of each endothelial cell subclusters for HCC3, HCC4, and HCC5. **f** Bubble plot showing the intercellular communications among HCC cell, endothelial cell, and immune cell subpopulations, with each bubble denoting the cell identity and line thickness denoting the strength of intercellular interactions. **g** Circos plot showing intercellular communication network of each HCC cell, endothelial cell, and immune cell subpopulations with a high confidence level, with each arrow denoting the interaction between the source cell ligand and target cell receptor, and the arrow thickness denoting the number of ligand-receptor interaction pairs. **h** Heatmap representing the average expression of ecological niche genes of angiogenesis at the single-cell level. See also Supplementary Fig. 4 and Supplementary Table 8.

4d). Our analysis identified the angiogenesis niche genes were strongly expressed at the transcriptome, proteome, single-cell, and bulk level (Fig. 7h, Supplementary Fig. 4e).

We integrated the bulk transcriptome data into an independent cohort of 7269 HCC patients from the databases of Cancer Genome Atlas Liver Hepatocellular Carcinoma (TCGA-LIHC), International Cancer Genome Consortium Liver Cancer-RIKEN, JP (ICGC-LIRI-JP) cohort and Gene Expression Omnibus (GEO) to establish an angiogenesis score based on the angiogenesis niche gene set (Supplementary Fig. 4f), which was validated has predictive potential of undesirable overall survival (Supplementary Fig. 4g).

Unique ecological niche of rapid HCC recurrence

Hepatectomy is the most effective treatment for HCC patients, whereas high recurrence rate (50–70% at 5 years) yields a poor long-term survival[15]. The relevant spatiotemporal molecular patterns of recurrence are poorly understood. At the cut-off time of this study, recurrence occurred in Patients#2 and #5. In particular, Patient#2 experienced rapid recurrence within 2 months after surgery. Therefore, this case aroused our strong interest. Firstly, the main functional blocks on the spatial map of Patient#2 were identified, including tumor invasion and metastasis (EMT and focal adhesion) and hypoxia (HIF-1 signaling) regions (Fig. 8a). Despite invasion and metastasis-related regions were identified on the spatial maps from all the patients, Patient#2 and Patient#5 not only possessed the aforementioned characteristics but also shared an active functional region of hypoxia-related pathways, suggesting a stronger potential for recurrence in these patients. Notably, Patient#2 showed considerably lower angiogenesis activity than Patient#5 (Supplementary Fig. 1a), but experienced recurrence earlier. To further explore this phenomenon, we extracted cell subpopulations of Patient#2, obtaining a total of 54 cell clusters (Fig. 8b) and identifying the ecological niche genes of rapid HCC recurrence (i.e., genes expressed in HCC cells and most other cells of Patient#2 but hardly expressed in other patients) (Fig. 8c). The expression distribution of these genes in the single-cell and spatial resolutions were uniformly and strongly expressed, and exhibited the spatiotemporal consistency at the genome-transcriptome-proteome level, suggesting a potential regulatory role in the rapid recurrence of HCC (Fig. 8d, e, Supplementary Fig. 5a). Based on Fig. 8b–d and literature review, we discovered that keratin 8 *(KRT8)*, keratin 18 (*KRT18*), and keratin 20 (*KRT20*) genes are associated with high aggressiveness in the rapid recurrence of HCC[64–66]. To further validate these specific rapid recurrence niche genes, immunohistochemistry (IHC) was conducted to assess the protein expression of *KRT8*, *KRT18*, and *KRT20* in HCC tissues from 32 rapid recurrence patients and 9 recurrence-free patients and the results revealed that the expression of *KRT8* ($P = 0.0272$), *KRT18* ($P = 0.0003$), and *KRT20* ($P = 0.0169$) were significantly increased in rapid recurrence patients compared to those with recurrence-free (Fig. 8f). These findings suggested that *KRT8*, *KRT18*, and *KRT20* were potential markers of HCC rapid recurrence.

External validation showed that the ecological niche genes of rapid HCC recurrence were significantly enriched in an independent cohort of patients with HCC from GEO compared to the control (Supplementary Fig. 5b). In addition, these genes were integrated for the generation of a relapse score, which was validated has predictive potential of undesirable overall survival (Supplementary Fig. 5c).

Discussion

Multiple HCC clinical staging systems have been proposed, but the accurate prediction of prognosis and guidance on treatment for HCC patients remain difficult due to the high degree of ITH contributing to the creation of complex tumor ecosystems[67,68]. Despite scRNA-seq is capable to characterize the heterogeneity of HCC on the temporal, but the research insights into the spatial heterogeneity remain limited[69–71]. Here, we developed a single cell-spatial-bulk global heterogeneity landscape and spatiotemporal dynamic evolution pattern of the ecosystem in HCC. ITH is the definite core driving force of tumor evolution and results in vastly different therapeutic responses[72,73]. In our study, molecular and functional heterogeneous HCC cell subclusters were adequately manifested at the spatial-single cell-bulk level, and consistently pervaded the genome–transcriptome–proteome–metabolome networks. Specific metabolites were observed shared among cirrhotic nodules, HCC lesions, paracancerous tissue, and peripheral blood in Patient#4, suggesting a relatively conservative trait in the parallel evolution of the cirrhotic nodules, HCC lesions in an individual. Our high-resolution multi-omics data demonstrated that the high degree of ITH was mainly attributed to genetic discrepancy among HCC cells.

We found most immune cell subpopulations were shared among all patients but their proportions were significant different, which is consistent with the findings of Sun et al. and Zhang et al. [72,73]. Besides, differential distributions of immune cells were clearly exhibited on the spatial maps. These results demonstrated the composition ratio and spatial distribution of immune cells specifically contributed to the immune heterogeneity, and implied the great importance of local microenvironment influence on tissue-specific remodeling of immune cells. In general, classically activated M1-TAMs executives multiple antitumor functions[74,75]. However, in this study, M1-TAMs were shown to have manifested high tumor-induced metabolic activities (i.e. amino acid metabolism and glycolysis)[23], with partial loss the primitive anti-tumor functions. Further, metabolic activities appeared to manifest higher diversification during the M2-TAMs polarization. These results mean that M1-TAMs were highly likely to obtain tumorigenic phenotypes through metabolic reprogramming in the context of HCC[23,76]. In addition, our observations that exhausted CD8$^+$ T, CD4$^+$ T, and Treg cell subpopulations exhibited consistent transcription signature of overexpressed immune checkpoint genes *CTLA4*, *PDCD1*, and *TIGIT* is in agreement with the findings of Fan et al.[15], showing a preponderant counting of cytotoxic CD8$^+$ T cells but the majority had degenerated into dysfunctional states of immunosuppression and apoptosis. This supports the generally poor anti-tumor response of different types of tumor-infiltrating lymphocytes (immune effector cells and regulatory cells), leading to the relatively limited therapeutic efficacy of immune checkpoint inhibitors for HCC[77,78].

Mounting evidence indicated that tumor cells possess the ability to shape environment for favors their growth[79,80]. In this study, we found that HCC cells are the core driving force for tumor evolution and actively release signals to reprogram various immune and stromal cells, especially taming TAMs as the most important hub cells of the network. In particular, M2-type TAMs promoted the development of exhausted CD8$^+$ T cells and Tregs through CD86-CTLA4 receptor/ligand interactions, which further accelerated the immunosuppression within the TME. This indicated that HCC cells drive the synergistic effects with surrounding immune cells to support

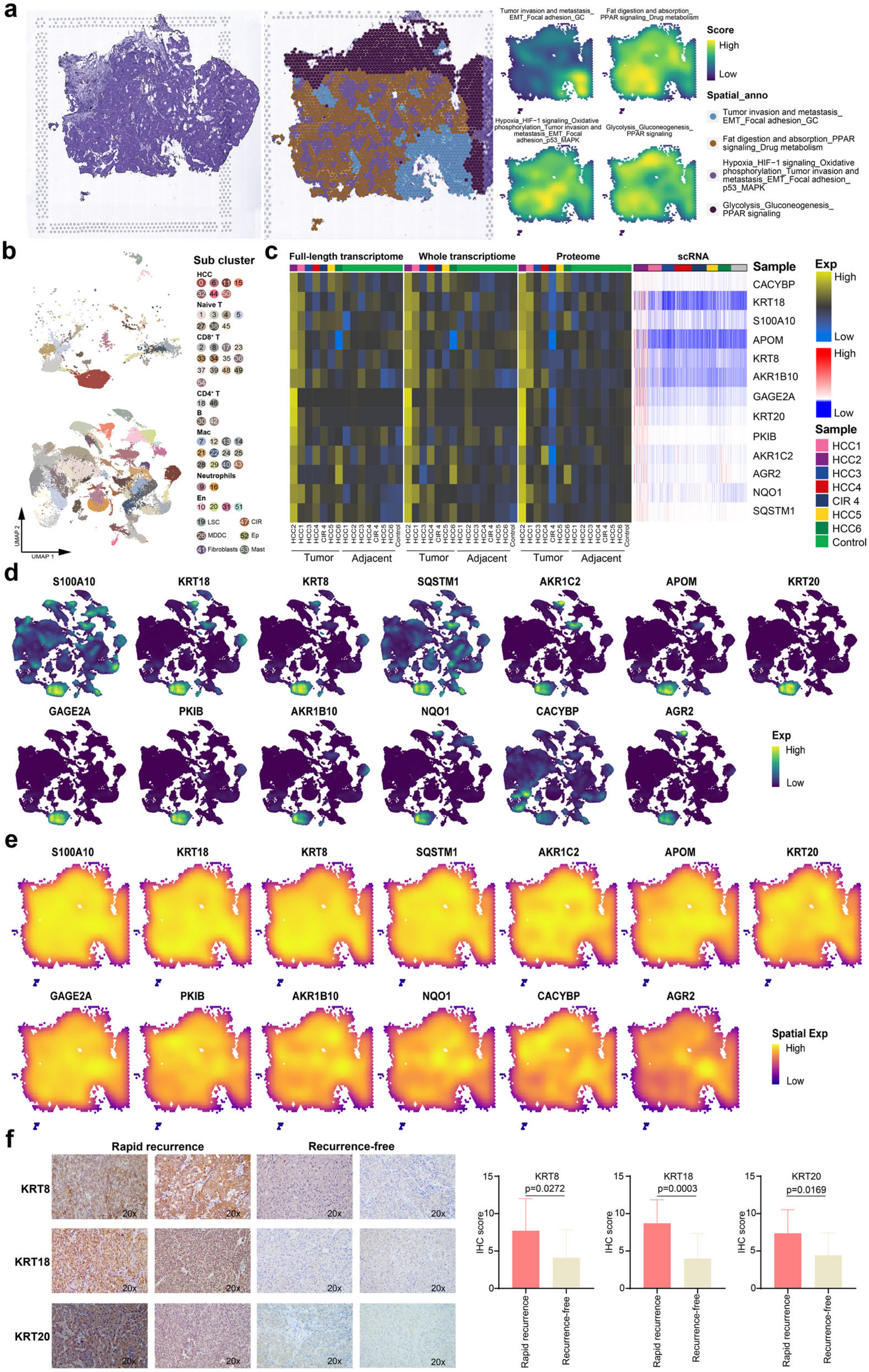

Fig. 8 | Ecological niche of early HCC recurrence. a H&E staining(left), and spatial cluster distribution of section (middle) labeled by colors, and density plots of specific gene sets of spatial cluster (right) for HCC2, defined into different spatial blocks. **b** UMAP plot showing the cell subclusters of HCC2 (top) and other tissues (bottom), labeling in different colors. **c** Heatmap representing the expression of ecological niche genes of HCC recurrence at the full-length transcriptome, whole transcriptome, proteome, and single-cell RNA levels. **d** UMAP plot showing the distribution of ecological niche genes of HCC recurrence. **e** Spatial feature plots showing the distribution of the ecological niche genes of HCC recurrence in HCC2. **f** Immunohistochemical staining showing increased KRT8, KRT18, and KRT20 expressions in the resected tumors originated from the rapid recurrence HCC patients compared to the recurrence-free HCC patients, original magnification, ×200. See also Supplementary Fig. 5.

tumor development. In most cases, liver cirrhotic lesions usually develop into dysplastic precancerous nodules through multistep molecular alteration and ultimately progress to early HCC[81,82]. We obtained valuable specimens of simultaneous cirrhosis and HCC in individual Patient#4 and showed the pattern of parallel evolution of these two types of lesions at the spatial and single-cell resolution for the first time. We identified the common progenitor cells of cirrhosis and HCC, and observed abundant hepatic disease signals and HCC signals were activated. This implied a molecular basis of the onset of HCC that genetic abnormalities had been accumulated before the malignant transformation. The immune cell types in HCC4 were extremely complex, with Mac and CD8$^+$ T cells possessing 9 and 11 phenotypes of each, respectively. Numerous studies have reported that hepatic Mac cells play important roles in the development and progression of hepatic diseases[83,84]. Consistent with the findings obtained from the global immune maps as described above, Macs still occupy the most important position in TIME of Patient#4. Development and differentiation of TAMs were far more complex in HCC lesions than in cirrhotic lesions: HCC4 was dominated by M1-TAMs, while they exhibited various metabolic reprogram activities and oncogenic phenotypes[76,85]. In contrast, the differentiation of TAMs around cirrhosis was relatively simple: CIR4 was dominated by M2-TAMs, but they maintained the tissue repair phenotype[86,87]. These results highlighted the great importance of different lesion cells in subverting macrophage function and eliciting discrepant transformation of the immune microenvironment. In this study, the primitive CD8$^+$ T cells were progressively positive for *GZMB*, *GNLY*, and thymopoietin *(TMPO)*, thus possessing cytotoxic effects. However, chronic viral infection and cancer are long-term diseases under the persistent antigen load[27,88], which ultimately forced cytotoxic CD8$^+$ T cells to gradually differentiate into CD8$^+$ T cells without immune killing, and meanwhile significantly up-regulated its inhibitory receptors (HAVCR2, CTLA4). The TCR signal pathways were observed significantly activated, which further demonstrates that persistent antigen involvement is a predominant factors affecting T cell exhaustion[89,90].

The spatial-temporal differentiation trajectory of CD8$^+$ T cells illustrated the dynamic game between pathological cells and immune cells. CD8$^+$ T cells around the two lesions had already manifested the characteristics with strong proliferation, cytotoxicity, and migration since the evolution origin, suggesting a barrier role of host immunity[91,92]; but that around HCC gradually transformed into more lasting and stronger immunosuppressive effect at the intermediate and later stages of evolution. Exhausted CD8$^+$ T cells in cirrhotic lesions reverted to cytotoxic IL7R$^+$CD8$^+$ T cells during the late stages of differentiation; however, recovery from exhaustion was not observed in HCC lesions. These phenomena once again strongly suggest that different types of lesions exert different effects on the surrounding immune environment. Most cytotoxic CD8$^+$ T cells surrounding HCC cells had been weakening their effective immune response, but through the fine-tuning of the effects to promote the evolution of the lesions at different stages instead[91,92]. Notably, we found that HCC cells directly tamed exhausted CD8$^+$ T cells through strong co-inhibitory signals provided by the HAVCR2-LGALS9 and CD86-CTLA4 axes. This was validated on spatial transcriptomic maps, indicating the prominent contributions of these receptor-ligand axes in shaping the immunosuppressive maps of HCC. Our findings suggest that the interactions between lesion cells and immune cells during the evolution process of CIR and HCC favor the transformation process towards better survival fitness through the continuous modification of immune cells, thereby providing a "safe haven" for lesion cells.

Angiogenesis serves as a vital pathological basis for carcinogenesis and progression[93,94]. In this study, only four En subpopulations were identified from all the patients, among them pathway enrichment analysis revealed a high similarity of the functional pathways, indicating the existence of a certain level of phenotypic conservatism in the endothelium among HCC patients. Furthermore, we observed En subpopulations were subjected to cascade regulation, with HCC acting as the emitter and TAMs as the amplifier, indicating that the greater heterogeneity of Ens stemmed from reprogramming by HCC cells.

High recurrence is the main factor that affects the unfavorable outcome of HCC patients who have undergone curative surgery[82,95]. Although Patients#5 possessed high-risk factors for recurrence such as higher angiogenic activity and larger tumor size, Patients#2 experienced earlier recurrence, indicating the presence of heterogeneity in the ecology of HCC recurrence. We identified a series of ecological niche genes of rapid HCC recurrence with prognostic significance. These genes were unique to Patient#2 and characterized by the high level of consistency in expression on the spatiotemporal scale, manifesting an abundance of proliferative and invasive functions. In particular, numerous members of the keratin protein family genes (*KRT8*, *KRT18*, *KRT20*) were overexpressed, reflecting the high aggressiveness of HCC cells in this patient[65,66,96]. Subsequently, we validated the expression of these specific rapid recurrence niche genes in HCC patient samples by IHC. The results showed that *KRT8*, *KRT18*, and *KRT20* were significantly overexpressed in patients with rapid recurrences of HCC compared with recurrences-free (all $P < 0.05$). Therefore, these genes may serve as marker genes of HCC rapid recurrence. In essence, we preliminarily depicted a potential molecular landscape of HCC rapid recurrence. This malignant trait is mainly dominated by the natural selection of HCC cells, once again demonstrating the fact that the ITH is primarily determined by HCC cells.

In the present study, we constructed single cell-spatial-bulk global heterogeneity landscapes and spatiotemporal dynamic evolution of the ecosystem in HCC, indicating that HCC cells possessing morphological diversity and flexible phenotypic plasticity, are the core driving force for generating ITH and shaping the tumor environment. Also, we deeply explored the parallel evolution of cirrhosis and HCC, the unique vascular ecology, and rapid recurrence ecology. Our data are valuable resource in further in-depth analysis of the intricate relationships between the spatiotemporal heterogeneity of HCC and various clinical scenarios, and the development of individualized precision diagnostic and treatment strategies for HCC patients in clinical practice.

Methods

Human subject

In this study, seven lesion tissue samples (six HCC tissue samples and one cirrhotic tissue sample) and preoperative blood samples were collected from six patients with pathological diagnosis of HCC at different clinical stages from the Guangxi Medical University Cancer Hospital. A non-carcinoma liver tissue and blood samples were obtained from one patient (control donor) who underwent surgical resection for hepatic hemangioma were used as control. The study was conducted under the approval (Approval No. LW2022040) of the ethics review committee of the Guangxi Medical University Cancer Hospital and has complied with all relevant ethical regulations including the Declaration of Helsinki. All included patients gave their informed consent to participate. Consent for publication was obtained from all participants.

Hematoxylin-eosin staining and immunohistochemical staining

The tissues of the patients were collected and immediately fixed with 10% formaldehyde for 12 h. After dehydration, transparency, paraffin embedding, and sectioning (4 µm), they were used for H&E and IHC. All the staining process was carried out following the manufacturer's instruction. H&E stained sections were made under an optical microscope (OLYMPUS BX43) using an eyepiece ×10 and objective lens ×40 imaging and capturing images on ImageView 4.15 (Pooher) software. Immunohistochemical sections were scanned with a Pannoramic Digital Slide Scanner (3DHISTECH). All sections were evaluated by two pathologists without knowing patient's clinical characteristics and outcomes.

The following primary antibodies were used to bind specific IHC proteins: CRP (Bioss, bs-0155R), LGALS4 (Abways, CY7043), NPW (Bioss, bs-11531R), IFI27 (Affinity, DF8989), CYP2E1 (Bioss, bs-4562R), SAA1 (Bioss, bs-19359R), CA4 (R&D Systems, MAB2186-SP), CYP2E1 (Bioss, bs-4562R), IDO1(Bioss, bs-15493R), HOXD9 (Bioss, bs-8603R), ANGPT2 (Bioss, bs-0677R) and FLT1 (Bioss, bs-0170R), KRT8 (Bioss, bsm-52419R), KRT18 (Bioss, bs-2043R), KRT20 (Bioss, bsm-52060R), and secondary antibody was Horse Anti-Mouse/Rabbit IgG (Vector, ZF1028). The raw data from 32 rapid recurrence patients and 9 recurrence-free patients of HCC has been uploaded (Supplementary file 1).

Multi-omics sequencing

All sequencing of this study was carried out by the BMKcloud (Biomarker Technologies Corporation, Beijing, China).

Spatial transcriptome sequencing

We performed RNA extraction on frozen embedded tissues stored at −80 °C to get the RNA and subsequently test its quality. RNA integrity number (RIN) value ≥ 7, 28S/18S is 1.8–2.0, which indicates that the extracted RNA has good integrity and basically no degradation. Then, tissue optimization was carried out to test whether the samples were suitable for spatial transcription experiments to explore the optimal penetration time. Tissue permeabilization and mRNA reverse transcription were carried out in order to create cDNA, which was then followed by the synthesis and denaturation of the second strand of cDNA in accordance with the permeabilization time established by tissue optimization. By using the qPCR method, the cycle number of the cDNA amplification was identified, and the cDNA was then purified and quality checked. The gene expression library was constructed. The Illumina NovaSeq 6000 was used to sequence the Visium spatial gene expression library once it passed the quality check. The original image file obtained offline is converted into Sequenced Reads by CASAVA through Base Calling, stored in fastq format, and the official 10× Genomics software SpaceRanger is used for data comparison, gene quantification, and site identification.

Single-cell RNA sequencing

Following the guidelines of the 10× Genomics Single Cell 3’v3.1 kit (Cat# PN-1000269, 10× Genomics), we prepared the samples and created the cDNA library. In short, through microfluidic technology, single cells and reagents required for reaction are wrapped in GEM droplets together with glue beads with cell tag sequence (cell Barcode) on the chip, collect the GEMs droplets containing cells. In the GEM droplets, the cells lyse and release mRNA, which combines with the cell Barcode primer on the bead to complete the reverse transcription reaction. Then GEMs were broken, cDNA was recovered and enriched by PCR amplification, and a cDNA library was constructed. The insert fragment size of the cDNA library was detected by Qseq400 biological analyzer to confirm that the insert fragment size was qualified, the peak type was single, there was no heteropeak, no splice, and no primer dimer. The cDNA product and library concentration were detected based on Qubit 4.0 fluorescence quantitative instrument. The Illumina NovaSeq 6000 platform was then used to sequence the sample library. The original picture files acquired offline are converted by CASAVA through Base Calling into sequenced reads and stored in fastq format. The sequencing results are then compared and quantified using CellRanger, the official 10× Genomics software.

Full exon sequencing

According to the instructions of Nimblegen Seqcap Ez Exome Enrichment Kit V3 a library of 180–220 bp inserted fragments was constructed. After the construction of the library is completed, Qubit 3.0 was utilized for its preliminary quantification, and for the detection of its insert size, we used Agilent 2100. Then, qPCR was performed for accurate quantification of the effective library concentration (which was more than 3 nm), and the library inspection was completed. After the library inspection is qualified, the two-terminal sequencing of the Illumina HiSeq platform is carried out based on the effective library concentration and the amount of target offline output data. The original image file obtained from off-line is transformed into the original sequencing sequence (Sequenced Reads) and stored in fastq format. Then, data filtering is carried out, including removing the sequence of adapter, removing the reads with N content greater than 10% and removing the reads with a base quality value lower than 10 more than 50%, and finally obtaining Clean Reads. The filtered high-quality reads were compared with the human reference genome sequence (UCSC hg19) using BWA software[97], and then used for subsequent information analysis.

Whole transcriptome sequencing

Each sample’s total RNA was isolated using Trizol (Thermo Fisher Scientific). The Ribo-Zero rRNA Removal Kit (Cat# RZH1046, Epicentre) was used to remove rRNA from 1.5 μg of total RNA from each sample. The NEBNextR UltraTM-directed RNA library preparation kit for IlluminaR (NEB) was used to generate the sequencing library as per the manufacturer’s instructions and each sample’s attribute sequence had the index code added to it. As per the manufacturer’s recommendations, the TruSeq PE Cluster Kitv3-cBot-HS (Illumia) was used on the acBot Cluster Generation System to cluster the index-coded sample data. We sequenced the library preparations on an Illumina Hiseq platform after cluster creation, and paired-end reads were produced. Internal Perl scripts were used to initially handle raw reads in fastq format. In the meanwhile, the clean data’s Q20, Q30, GC content, and sequence repeat level were determined. As per the readings that were mapped to the reference genome, the transcriptome was then put together using StringTie[98]. Utilizing the gffcompare program[99], the assembled transcripts were annotated. CPC2/CNCI/Pfam/CPAT, which can identify protein-coding genes, was utilized for additional screening on transcripts longer than 200 nt and having more than two exons.

Full-length transcriptome sequencing

The cDNA PCR sequencing kit (SQK-PCS109) (Cat# SQK-PCS109, Oxford Nanopore) produced by Oxford nanopore (ONT) technologies was used to prepare the total RNA for the cDNA library. Simply put, the reverse transcriptase’s template conversion activity enhanced the full-length cDNA and appended the designated PCR adapter to both ends of the initial strand of cDNA. Using LongAmp labeling from NEB, fourteen cycles of cDNA-PCR were run. T4 DNA ligase (NEB) was then used to splice the PCR results. Agencourt XP beads are employed for DNA purification in accordance with the ONT procedure. On the PromethION platform, the last cDNA library was added to FLO-MIN109 flowcells. In the MinKNOW2.2 software package, base calling is used to transform fast5 format data into fastq format for storage. The reference genome was then compared to the full-length sequence using the minimap2 program[100]. After clustering by comparison information, the consistent sequence was obtained by pinfish software. Using minimap2, the consistent sequences from each sample were combined and matched to the reference genome. The findings were de redundant. The sequences with identity and coverage less than 0.9 and 0.85, respectively, were screened, and the comparisons with only 5 ‘exon differences were merged.

Proteome sequencing

According to the experimental requirements, protein extraction, digestion, and TMT labeling were performed. The obtained peptide fractions were then divided into 20 μL buffer A (0.1% FA, 2% ACN) and were suspended and centrifuged at 12,000 rpm for 10 min. Nanoflow HPLC system (Thermo Scientific) and Orbitrap Fusion Lumos mass spectrometer (Thermo Scientific) were used to inject the 10 μL supernatant. Separate the sample using the EASY-Spray C18 column after loading it onto the Acclaim PepMap100 C18 column. In Orbitrap, the mass spectrometer conducts complete MS scanning in the 300–1500 *m/z* range with a 120,000 resolution while operating in positive ion mode (source voltage 2.1 kV). For MS/MS scanning, after a full MS scanning, the 20 most prevalent ions with different charge states are chosen for higher energy collision dissociation fragmentation. The database used in this experiment is the Uniprot HUMAN database (downloaded on April 20, 2019). Proteome Discoverer 1.4 was used to process MS/MS data.

Metabolome sequencing

From patient tissue and blood samples, metabolites were isolated, and supernatants were separated for sequencing. The liquid chromatography-mass spectrometry system for metabolomics analysis is composed of ultrahigh performance liquid chromatography Acquity I-Class PLUS in series with Waters high-resolution mass spectrometer Xevo G2-XS QTOF. The Acquity UPLC HSS T3 chromatographic column (1.8 μm 2.1*100 mm) (Cat # 186003538) used is purchased from Waters. Waters Xevo G2-XS QTOF high-resolution mass spectrometer collects primary and secondary mass spectrometry data in MSe mode under the direction of acquisition software (MassLynx V4.2, Waters). The Progenesis QI program then processes the original data for peak extraction, peak calibration, and other data processing operations. On the basis of the online METLIN database[101] of the Progenesis QI software and the self-built database of BmK, the original data is then recognized. The mass number variation of the parent ion is within 100 ppm, while the fragment ion's mass number deviation is within 50 ppm, according to theoretical fragment identification. Follow-up analysis is performed after adjusting the initial peak area data to the overall peak area.

Generation of the single-cell map and cell-type annotation

The construction of single-cell profiles was performed using the R language "Seurat" package[102]. Double cells were first filtered with "DoubletFinder" (based on the official 10x Assuming 7.5% doublet formation rate) nFeature_RNA > 400 and percent.mt < 20. Next, all single cell data were integrated using the "IntegrateData" function, and the "FindNeighbors" and "FindClusters" functions for cell clustering and identification of cell clusters. The clustering results were uniformly downscaled and visualized using a consistent stream approximation and projection for dimensionality reduction (UMAP) algorithm[103] to generate single-cell profiles. In addition, marker genes for each cell cluster were identified using the "FindAllMarkers" function. Ultimately, cell cluster types were defined and annotated to the single-cell atlas based on the classical markers of cells identified by single-cell sequencing, in the laboratory and in the clinic.

Generation of spatial transcriptional profiles

For the spot gene expression matrix generated by "Space Ranger", we first performed a conventional statistical analysis, i.e., we calculated the number of unique molecular identifiers (UMIs) and genes detected in each spot. On this basis, the data were normalized by "SCTransform"[104] as well as detecting highly variable features, and stored in the SCT assay. Subsequently, the data were downscaled and clustered using the same workflow as for the scRNA-seq analysis. Ultimately, the results of the clustering were visualised using "DimPlot" in UMAP space or using "SpatialDimPlot".

Estimation of copy number variation in single cells

Single-cell CNV was estimated by copy number karyotype analysis (CopyKAT) of aneuploid tumors[105]. By integrating the Bayesian technique with hierarchical clustering, CopyKAT determines the subclonal structure and estimates the genome copy number distribution of a CellRanger.

Pathway enrichment analysis of Kyoto Encyclopedia of Genes and Genomes

The Kyoto Encyclopedia of Genes and Genomes (KEGG) pathway enrichment analysis was carried out by using the R software package "clusterProfiler"[106]. The pathway with $P < 0.05$ was considered significant.

Gene set enrichment analysis

Gene set enrichment analysis was carried out on the identified recurrent niche genes using the ClusterProfiler package. $P < 0.05$ was considered to be significant.

Quasi temporal analysis

The quasi-temporal analysis is carried out by using the R language package "Monocle 3"[107]. Through quasi-temporal analysis, the differentiation and development trajectories of immune cell subpopulations in HCC patients and the evolutionary trajectories of HCC and CIR cell subclones were constructed, and the results were visualized by the UMAP method. In addition, based on the graph test function of Monocle 3, pseudo-time-related genes, i.e. genes whose expression changes with the clonal evolution of HCC, were identified, and pseudo-time related genes with a false discovery rate less than 0.05 were chosen for cluster heat map visualization.

Spatial trajectory inference

Spatial trajectory inference is based on stlearn's pseudo-space-time (PST) trajectory analysis algorithm[108]. PST is a development of the widely known pseudo-time concept commonly used in the analysis of scRNA-seq data. It aims to identify biological processes based on the gradient changes in tissue transcription status. Firstly, PAGA35, which is based on the whole tissue Spatial Morphological gene Expression normalization, gene expression data was used for trajectory analysis to find the connections within the cluster. Next, the pseudo time is calculated by the diffusion pseudo time method[109]. In this study, the subclones of hepatic progenitor cells based on pseudo-temporal analysis were defined as roots, and then the pseudo-space-time distance (PSTD) was calculated. In order to determine the shortest, rooted tree and branch (trajectory) of the nodes in the connection graph, we built a directed graph using the adjusted PSTD matrix and optimized it using the directed minimum spanning tree algorithm.

Gene regulatory network

The GRN with transcription factors as the core was implemented using Python module tool pySCENIC[110].The workflow of the tool begins with a counting matrix that describes the cells' gene abundance, including three stages. The coexpression module is first inferred using each objective regression method (GRNBoost2). Next, utilizing cis-regulatory motif discovery (cisTarget), indirect targets are removed from these modules. The enrichment fraction of the regulator target gene (AUCell) was finally used to measure the activity of these regulators. The nonlinear projection approach may be used to represent the visual grouping of cells on the basis of the cell activity patterns of these regulators.

Cell communication analysis

Cell communication analysis was performed using the R language iTALK package[111]. In order to uncover significant intercellular communication events, ITALK identifies highly expressed or differentially expressed genes in cell clusters, and matches and pairs these genes through the ligand-receptor database.

Gene set score estimation and survival analysis

The scores of the angiogenic niche gene set and recurrent niche gene set of HCC patients were calculated by using the AddModuleScore function of the Seurat package. Subsequently, in order to evaluate the prognostic efficacy of gene set scores for HCC, survminer[112] an R language package, was used for survival analysis.

Data analysis and statistics

All Bioinformation analysis in our research is based on the Bioinforcloud platform (http://www.bioinforcloud.org.cn).

Data availability

The accession number for the processed expression data of scRNA-seq, ST-seq, whole exome sequencing, whole transcriptome sequencing, full-length transcriptome sequencing, proteome sequencing, and non-targeted metabolomics sequencing reported in this paper is HRA002748 (https://ngdc.cncb.ac.cn/gsa-human/browse/HRA002748). Further information and requests for reagents should be directed to and will be fulfilled by the Lead Contact, Rong Liang (email: liangrong@gxmu.edu.cn).

Received: 27 January 2024; Accepted: 30 October 2024;

References

1. Craig, A. J., von Felden, J., Garcia-Lezana, T., Sarcognato, S. & Villanueva, A. Tumour evolution in hepatocellular carcinoma. *Nat. Rev. Gastroenterol. Hepatol.* **17**, 139–152 (2020).

2. Nguyen, P. H. D. et al. Intratumoural immune heterogeneity as a hallmark of tumour evolution and progression in hepatocellular carcinoma. *Nat. Commun.* **12**, 227 (2021).
3. Qi, F. et al. Comprehensive metabolic profiling and genome-wide analysis reveal therapeutic modalities for hepatocellular carcinoma. *Res.* **6**, 0036 (2023).
4. Liang, R. et al. Mechanism and molecular network of RBM8A-mediated regulation of oxaliplatin resistance in hepatocellular carcinoma. *Front. Oncol.* **10**, 585452 (2020).
5. Kalasekar, S. M., VanSant-Webb, C. H. & Evason, K. J. Intratumor heterogeneity in hepatocellular carcinoma: challenges and opportunities. *Cancers* **13**, https://doi.org/10.3390/cancers13215524 (2021).
6. Zhai, W. et al. The spatial organization of intra-tumour heterogeneity and evolutionary trajectories of metastases in hepatocellular carcinoma. *Nat. Commun.* **8**, 4565 (2017).
7. Vitale, I., Shema, E., Loi, S. & Galluzzi, L. Intratumoral heterogeneity in cancer progression and response to immunotherapy. *Nat. Med.* **27**, 212–224 (2021).
8. Vessoni, A. T., Filippi-Chiela, E. C., Lenz, G. & Batista, L. F. Z. Tumor propagating cells: drivers of tumor plasticity, heterogeneity, and recurrence. *Oncogene* **39**, 2055–2068 (2020).
9. Liggett, L. A. & DeGregori, J. Changing mutational and adaptive landscapes and the genesis of cancer. *Biochim. Biophys. Acta Rev. Cancer* **1867**, 84–94 (2017).
10. Janiszewska, M. The microcosmos of intratumor heterogeneity: the space-time of cancer evolution. *Oncogene* **39**, 2031–2039 (2020).
11. da Silva-Diz, V., Lorenzo-Sanz, L., Bernat-Peguera, A., Lopez-Cerda, M. & Muñoz, P. Cancer cell plasticity: impact on tumor progression and therapy response. *Semin. Cancer Biol.* **53**, 48–58 (2018).
12. Smith, P. E. & Mucklow, J. C. Writing clinical scenarios for clinical science questions. *Clin. Med.* **16**, 142–145 (2016).
13. Katzenelenbogen, Y. et al. Coupled scRNA-Seq and intracellular protein activity reveal an immunosuppressive role of TREM2 in cancer. *Cell* **182**, https://doi.org/10.1016/j.cell.2020.06.032 (2020).
14. Rao, A., Barkley, D., França, G. S. & Yanai, I. Exploring tissue architecture using spatial transcriptomics. *Nature* **596**, 211–220 (2021).
15. Sun, Y. et al. Single-cell landscape of the ecosystem in early-relapse hepatocellular carcinoma. *Cell* **184**, https://doi.org/10.1016/j.cell.2020.11.041 (2021).
16. Zhang, Q. et al. Landscape and dynamics of single immune cells in hepatocellular carcinoma. *Cell* **179**, https://doi.org/10.1016/j.cell.2019.10.003 (2019).
17. Andreis, P. G. et al. Neuropeptides B and W enhance the growth of human adrenocortical carcinoma-derived NCI-H295 cells by exerting MAPK p42/p44-mediated proliferogenic and antiapoptotic effects. *Int. J. Mol. Med.* **16**, 1021–1028 (2005).
18. Lao, M. et al. Regulator of calcineurin 1 gene isoform 4 in pancreatic ductal adenocarcinoma regulates the progression of tumor cells. *Oncogene* **40**, 3136–3151 (2021).
19. Cai, Z. et al. Galectin-4 serves as a prognostic biomarker for the early recurrence/metastasis of hepatocellular carcinoma. *Cancer Sci.* **105**, 1510–1517 (2014).
20. Yuan, R.-H. et al. Opposite roles of human pancreatitis-associated protein and REG1A expression in hepatocellular carcinoma: association of pancreatitis-associated protein expression with low-stage hepatocellular carcinoma, beta-catenin mutation, and favorable prognosis. *Clin. Cancer Res.* **11**, 2568–2575 (2005).
21. Sun, X. et al. Metallothionein-1G facilitates sorafenib resistance through inhibition of ferroptosis. *Hepatology* **64**, 488–500 (2016).
22. Hilmi, M. et al. Angiogenesis and immune checkpoint inhibitors as therapies for hepatocellular carcinoma: current knowledge and future research directions. *J. Immunother. Cancer* **7**, 333 (2019).
23. Li, S. et al. Metabolism drives macrophage heterogeneity in the tumor microenvironment. *Cell Rep.* **39**, 110609 (2022).
24. Raines, L. N. et al. PERK is a critical metabolic hub for immunosuppressive function in macrophages. *Nat. Immunol.* **23**, 431–445 (2022).
25. Yan, J. & Horng, T. Lipid metabolism in regulation of macrophage functions. *Trends Cell Biol.* **30**, 979–989 (2020).
26. Kelly, B. & Pearce, E. L. Amino assets: how amino acids support immunity. *Cell Metab.* **32**, 154–175 (2020).
27. Philip, M. & Schietinger, A. CD8 T cell differentiation and dysfunction in cancer. *Nat. Rev. Immunol.* **22**, 209–223 (2022).
28. Zhou, J., Wang, W. & Li, Q. Potential therapeutic targets in the tumor microenvironment of hepatocellular carcinoma: reversing the protumor effect of tumor-associated macrophages. *J. Exp. Clin. Cancer Res.* **40**, 73 (2021).
29. Moon, A. M., Singal, A. G. & Tapper, E. B. Contemporary epidemiology of chronic liver disease and cirrhosis. *Clin. Gastroenterol. Hepatol.* **18**, 2650–2666 (2020).
30. Kikuchi, M. et al. Genome-wide copy number variation analysis of hepatitis B infection in a Japanese population. *Hum. Genome Var.* **8**, 22 (2021).
31. Yin, X. et al. RUNX2 recruits the NuRD(MTA1)/CRL4B complex to promote breast cancer progression and bone metastasis. *Cell Death Differ.*, https://doi.org/10.1038/s41418-022-01010-2 (2022).
32. Su, G. et al. Enhancer architecture-dependent multilayered transcriptional regulation orchestrates RA signaling-induced early lineage differentiation of ESCs. *Nucleic Acids Res.* **49**, 11575–11595 (2021).
33. Tonc, E. et al. Unexpected suppression of tumorigenesis by c-MYC via TFAP4-dependent restriction of stemness in B lymphocytes. *Blood* **138**, 2526–2538 (2021).
34. Mauri, F. et al. NR2F2 controls malignant squamous cell carcinoma state by promoting stemness and invasion and repressing differentiation. *Nat. Cancer* **2**, 1152–1169 (2021).
35. Dong, L.-Q. et al. Heterogeneous immunogenomic features and distinct escape mechanisms in multifocal hepatocellular carcinoma. *J. Hepatol.* **72**, 896–908 (2020).
36. Kurebayashi, Y. et al. Immunovascular classification of HCC reflects reciprocal interaction between immune and angiogenic tumor microenvironments. *Hepatology* **75**, 1139–1153 (2022).
37. Willenborg, S. et al. Mitochondrial metabolism coordinates stage-specific repair processes in macrophages during wound healing. *Cell Metab.* **33**, https://doi.org/10.1016/j.cmet.2021.10.004 (2021).
38. Jones, A. E. & Divakaruni, A. S. Macrophage activation as an archetype of mitochondrial repurposing. *Mol. Asp. Med.* **71**, 100838 (2020).
39. Vitale, I., Manic, G., Coussens, L. M., Kroemer, G. & Galluzzi, L. Macrophages and metabolism in the tumor microenvironment. *Cell Metab.* **30**, 36–50 (2019).
40. Si, M. & Lang, J. The roles of metallothioneins in carcinogenesis. *J. Hematol. Oncol.* **11**, 107 (2018).
41. Chowdhury, D. et al. Metallothionein 3 controls the phenotype and metabolic programming of alternatively activated macrophages. *Cell Rep.* **27**, https://doi.org/10.1016/j.celrep.2019.05.093 (2019).
42. Tauriello, D. V. F. et al. TGFβ drives immune evasion in genetically reconstituted colon cancer metastasis. *Nature* **554**, 538–543 (2018).
43. Shapouri-Moghaddam, A. et al. Macrophage plasticity, polarization, and function in health and disease. *J. Cell Physiol.* **233**, 6425–6440 (2018).
44. Avila-Ponce de León, U., Vázquez-Jiménez, A., Matadamas-Guzman, M., Pelayo, R. & Resendis-Antonio, O. Transcriptional and microenvironmental landscape of macrophage transition in cancer: a Boolean analysis. *Front Immunol.* **12**, 642842 (2021).
45. Christofides, A. et al. The complex role of tumor-infiltrating macrophages. *Nat. Immunol.*, https://doi.org/10.1038/s41590-022-01267-2 (2022).

46. Basant, A. et al. Aurora B kinase promotes cytokinesis by inducing centralspindlin oligomers that associate with the plasma membrane. *Dev. Cell* **33**, 204–215 (2015).
47. Cuvertino, S. et al. ACTB loss-of-function mutations result in a pleiotropic developmental disorder. *Am. J. Hum. Genet.* **101**, 1021–1033 (2017).
48. Wang, H. et al. MiR-29c-3p suppresses the migration, invasion and cell cycle in esophageal carcinoma via CCNA2/p53 axis. *Front. Bioeng. Biotechnol.* **8**, 75 (2020).
49. Dong, K. et al. FCER1G positively relates to macrophage infiltration in clear cell renal cell carcinoma and contributes to unfavorable prognosis by regulating tumor immunity. *BMC Cancer* **22**, 140 (2022).
50. Concetti, J. & Wilson, C. L. NFKB1 and cancer: friend or foe? *Cells* **7**, https://doi.org/10.3390/cells7090133 (2018).
51. Yang, X. et al. Essential contribution of a chemokine, CCL3, and its receptor, CCR1, to hepatocellular carcinoma progression. *Int J. Cancer* **118**, 1869–1876 (2006).
52. Boutilier, A. J. & Elsawa, S. F. Macrophage polarization states in the tumor microenvironment. *Int. J. Mol. Sci.* **22**, https://doi.org/10.3390/ijms22136995 (2021).
53. Weiskopf, K. et al. Engineered SIRPα variants as immunotherapeutic adjuvants to anticancer antibodies. *Science* **341**, 88–91 (2013).
54. Perillo, N. L., Pace, K. E., Seilhamer, J. J. & Baum, L. G. Apoptosis of T cells mediated by galectin-1. *Nature* **378**, 736–739 (1995).
55. Rubinstein, N. et al. Targeted inhibition of galectin-1 gene expression in tumor cells results in heightened T cell-mediated rejection; a potential mechanism of tumor-immune privilege. *Cancer Cell* **5**, 241–251 (2004).
56. McCracken, M. N., Cha, A. C. & Weissman, I. L. Molecular pathways: activating t cells after cancer cell phagocytosis from blockade of CD47 “Don’t Eat Me” signals. *Clin. Cancer Res.* **21**, 3597–3601 (2015).
57. Bonaventura, P. et al. Identification of shared tumor epitopes from endogenous retroviruses inducing high-avidity cytotoxic T cells for cancer immunotherapy. *Sci. Adv.* **8**, eabj3671 (2022).
58. Yang, L. et al. Transcriptome landscape of double negative T cells by single-cell RNA sequencing. *J. Autoimmun.* **121**, 102653 (2021).
59. Liu, X. et al. SMAD4, activated by the TCR-triggered MEK/ERK signaling pathway, critically regulates CD8 T cell cytotoxic function. *Sci. Adv.* **8**, eabo4577 (2022).
60. Nicoli, F., Paul, S. & Appay, V. Harnessing the induction of CD8 T-cell responses through metabolic regulation by pathogen-recognition-receptor triggering in antigen-presenting cells. *Front. Immunol.* **9**, 2372 (2018).
61. Das, S., Shapiro, B., Vucic, E. A., Vogt, S. & Bar-Sagi, D. Tumor cell-derived IL1β promotes desmoplasia and immune suppression in pancreatic cancer. *Cancer Res.* **80**, 1088–1101 (2020).
62. Chen, J. Y. et al. Hoxb5 marks long-term haematopoietic stem cells and reveals a homogenous perivascular niche. *Nature* **530**, 223–227 (2016).
63. Zhou, R.-H. et al. Vascular endothelial growth factor activation of sterol regulatory element binding protein: a potential role in angiogenesis. *Circ. Res.* **95**, 471–478 (2004).
64. Golob-Schwarzl, N. et al. High Keratin 8/18 ratio predicts aggressive hepatocellular cancer phenotype. *Transl. Oncol.* **12**, 256–268 (2019).
65. Baek, A., Son, S., Baek, Y. M. & Kim, D. E. KRT8 (keratin 8) attenuates necrotic cell death by facilitating mitochondrial fission-mediated mitophagy through interaction with PLEC (plectin). *Autophagy* **17**, 3939–3956 (2021).
66. Sirniö, P. et al. Systemic inflammation is associated with circulating cell death released keratin 18 fragments in colorectal cancer. *Oncoimmunology* **9**, 1783046 (2020).
67. Chidambaranathan-Reghupaty, S., Fisher, P. B. & Sarkar, D. Hepatocellular carcinoma (HCC): epidemiology, etiology and molecular classification. *Adv. Cancer Res.* **149**, 1–61 (2021).
68. Nault, J.-C. et al. Clinical impact of genomic diversity from early to advanced hepatocellular carcinoma. *Hepatology* **71**, 164–182 (2020).
69. Ho, D. W.-H. et al. Single-cell RNA sequencing shows the immunosuppressive landscape and tumor heterogeneity of HBV-associated hepatocellular carcinoma. *Nat. Commun.* **12**, 3684 (2021).
70. Wu, R. et al. Comprehensive analysis of spatial architecture in primary liver cancer. *Sci. Adv.* **7**, eabg3750 (2021).
71. Wang, Y.-F. et al. Spatial maps of hepatocellular carcinoma transcriptomes reveal spatial expression patterns in tumor immune microenvironment. *Theranostics* **12**, 4163–4180 (2022).
72. Zhai, W. et al. Dynamic phenotypic heterogeneity and the evolution of multiple RNA subtypes in hepatocellular carcinoma: the PLANET study. *Natl. Sci. Rev.* **9**, nwab192 (2022).
73. Ma, L. et al. Single-cell atlas of tumor cell evolution in response to therapy in hepatocellular carcinoma and intrahepatic cholangiocarcinoma. *J. Hepatol.* **75**, 1397–1408 (2021).
74. Chen, Y. et al. Tumor-associated macrophages: an accomplice in solid tumor progression. *J. Biomed. Sci.* **26**, 78 (2019).
75. Wang, S. et al. Metabolic reprogramming of macrophages during infections and cancer. *Cancer Lett.* **452**, 14–22 (2019).
76. Mehla, K. & Singh, P. K. Metabolic regulation of macrophage polarization in cancer. *Trends Cancer* **5**, 822–834 (2019).
77. Sangro, B., Sarobe, P., Hervás-Stubbs, S. & Melero, I. Advances in immunotherapy for hepatocellular carcinoma. *Nat. Rev. Gastroenterol. Hepatol.* **18**, 525–543 (2021).
78. Sperandio, R. C., Pestana, R. C., Miyamura, B. V. & Kaseb, A. O. Hepatocellular carcinoma immunotherapy. *Annu. Rev. Med.* **73**, 267–278 (2022).
79. McGranahan, N. & Swanton, C. Clonal heterogeneity and tumor evolution: past, present, and the future. *Cell* **168**, 613–628 (2017).
80. Myojin, Y. et al. Hepatic stellate cells in hepatocellular carcinoma promote tumor growth via growth differentiation factor 15 production. *Gastroenterology* **160**, 1741–1754.e16 (2021).
81. Takeda, H. et al. Genetic landscape of multistep hepatocarcinogenesis. *Cancers* **14**, 568 (2022).
82. Yang, J. D. et al. A global view of hepatocellular carcinoma: trends, risk, prevention and management. *Nat. Rev. Gastroenterol. Hepatol.* **16**, 589–604 (2019).
83. Dou, L., Shi, X., He, X. & Gao, Y. Macrophage phenotype and function in liver disorder. *Front. Immunol.* **10**, 3112 (2019).
84. Wen, Y., Lambrecht, J., Ju, C. & Tacke, F. Hepatic macrophages in liver homeostasis and diseases-diversity, plasticity and therapeutic opportunities. *Cell Mol. Immunol.* **18**, 45–56 (2021).
85. Azizi, E. et al. Single-cell map of diverse immune phenotypes in the breast tumor microenvironment. *Cell* **174**, 1293–1308.e36 (2018).
86. Biswas, S. K. & Mantovani, A. Orchestration of metabolism by macrophages. *Cell Metab.* **15**, 432–437 (2012).
87. Grønbæk, H., Gantzel, R. H., Laursen, T. L., Kazankov, K. & Møller, H. J. Macrophage markers and innate immunity in cirrhosis. *J. Hepatol.* **73**, 1586–1588 (2020).
88. Melenhorst, J. J. et al. Decade-long leukaemia remissions with persistence of CD4 CAR T cells. *Nature* **602**, 503–509 (2022).
89. Yates, K. B. et al. Epigenetic scars of CD8 T cell exhaustion persist after cure of chronic infection in humans. *Nat. Immunol.* **22**, 1020–1029 (2021).
90. Vardhana, S. A. et al. Impaired mitochondrial oxidative phosphorylation limits the self-renewal of T cells exposed to persistent antigen. *Nat. Immunol.* **21**, 1022–1033 (2020).
91. Jiang, R. et al. The long noncoding RNA lnc-EGFR stimulates T-regulatory cells differentiation thus promoting hepatocellular carcinoma immune evasion. *Nat. Commun.* **8**, 15129 (2017).
92. Lebossé, F. et al. CD8T cells from patients with cirrhosis display a phenotype that may contribute to cirrhosis-associated immune dysfunction. *EBioMedicine* **49**, 258–268 (2019).

93. Morse, M. A. et al. The role of angiogenesis in hepatocellular carcinoma. *Clin. Cancer Res.* **25**, 912–920 (2019).
94. Ye, J. et al. Integrating single-cell and spatial transcriptomics to uncover and elucidate GP73-mediated pro-angiogenic regulatory networks in hepatocellular carcinoma. *Research* **7**, 0387 (2024).
95. Villanueva, A. Hepatocellular carcinoma. *N. Engl. J. Med.* **380**, 1450–1462 (2019).
96. Werner, S., Keller, L. & Pantel, K. Epithelial keratins: Biology and implications as diagnostic markers for liquid biopsies. *Mol. Asp. Med.* **72**, 100817 (2020).
97. Li, H. Aligning sequence reads, clone sequences and assembly contigs with BWA-MEM. *arXiv: Genomics* (2013).
98. Pertea, M. et al. StringTie enables improved reconstruction of a transcriptome from RNA-seq reads. *Nat. Biotechnol.* **33**, 290–295 (2015).
99. Pertea, G. & Pertea, M. GFF Utilities: GffRead and GffCompare. *F1000Research* **9**, https://doi.org/10.12688/f1000research.23297.2 (2020).
100. Li, H. Minimap2: pairwise alignment for nucleotide sequences. *Bioinformatics* **34**, 3094–3100 (2018).
101. Guijas, C. et al. METLIN: a technology platform for identifying knowns and unknowns. *Anal. Chem.* **90**, 3156–3164 (2018).
102. Butler, A., Hoffman, P., Smibert, P., Papalexi, E. & Satija, R. Integrating single-cell transcriptomic data across different conditions, technologies, and species. *Nat. Biotechnol.* **36**, 411–420 (2018).
103. Becht, E. et al. Dimensionality reduction for visualizing single-cell data using UMAP. *Nat. Biotechnol*, https://doi.org/10.1038/nbt.4314 (2018).
104. Hafemeister, C. & Satija, R. Normalization and variance stabilization of single-cell RNA-seq data using regularized negative binomial regression. *Genome Biol.* **20**, 296 (2019).
105. Gao, R. et al. Delineating copy number and clonal substructure in human tumors from single-cell transcriptomes. *Nat. Biotechnol.* **39**, 599–608 (2021).
106. Yu, G., Wang, L.-G., Han, Y. & He, Q.-Y. clusterProfiler: an R package for comparing biological themes among gene clusters. *OMICS* **16**, 284–287 (2012).
107. Trapnell, C. et al. The dynamics and regulators of cell fate decisions are revealed by pseudotemporal ordering of single cells. *Nat. Biotechnol.* **32**, 381–386 (2014).
108. Pham, D. et al. stLearn: integrating spatial location, tissue morphology and gene expression to find cell types, cell-cell interactions and spatial trajectories within undissociated tissues. *bioRxiv*, 2020.2005.2031.125658, https://doi.org/10.1101/2020.05.31.125658 (2020).
109. Haghverdi, L., Büttner, M., Wolf, F. A., Buettner, F. & Theis, F. J. Diffusion pseudotime robustly reconstructs lineage branching. *Nat. Methods* **13**, 845–848 (2016).
110. Van de Sande, B. et al. A scalable SCENIC workflow for single-cell gene regulatory network analysis. *Nat. Protoc.* **15**, 2247–2276 (2020).
111. Wang, Y. et al. iTALK: an R package to characterize and illustrate intercellular communication. *bioRxiv*, 507871, https://doi.org/10.1101/507871 (2019).
112. Kassambara, A., Kosinski, M., Biecek, P. & Fabian, S. Package 'survminer'. Drawing Survival Curves using 'ggplot2'(R package version *03 1)* (2017).

Acknowledgements

This work was supported by the Guangxi Natural Science Foundation (nos. 2024GXNSFDA010046, 2024GXNSFAA010401), National Natural Science Foundation of China (nos. 82060427, 82103297 and 82260548), Advanced Innovation Teams and XinghuScholars Program of Guangxi Medical University, Guangxi Medical University Outstanding Young Talents Training Program, Guangxi Scholarship Fund of Guangxi Education Department, Nanning Qingxiu District Science and Technology Project (nos. 2020037, 2020038, 2021007), Guangxi Medical and health key discipline construction project, Guangxi Medical and health key cultivation discipline construction project, Guangxi Key Laboratory of Basic and Translational Research for Colorectal Cancer, Youth Program of the Scientific Research Foundation of Guangxi Medical University Cancer Hospital (nos. 2021–06).

Author contributions

Conceptualization, R.L., J.Y., X.L., and Y.L.; Software J.Y., Y.L., Z.L., C.L., L.L., M.L., M.X., and H.Y.; Methodology, Y.L., X.G., C.L., J.H., Y.Li., J.Z., and X.L.; Investigation, X.G., L.Li. L.L., C.L., J.H., X.H., and S.H.; Formal Analysis, Z.L., Y.Li., H.Y., T.B., J.C., X.W., M.X., M.L., J.Z., F.W., G.W., L.M., B.X., X.L. and R.L.; Resources, J.Y., L.Li. T.B., J.C., X.W., F.W., G.W., L.M., and B.X.; Visualization, R.L., J.Y., Y.L. X.G., L.L., C.L., J.H., X.H., and S.H.; Writing-Original Draft, J.Y., and Y.L.; Writing-Review & Editing, X.L. and R.L.; X.L. and R.L provided overall supervision of the project.

Competing interests

The authors declare no competing interests.

Additional information

Supplementary information The online version contains supplementary material available at https://doi.org/10.1038/s41698-024-00752-1.

Correspondence and requests for materials should be addressed to Xiaoling Luo or Rong Liang.

Reprints and permissions information is available at http://www.nature.com/reprints